Yang Liu, An Deng, Mark Jaksa

Three-dimensional modeling of geocell-reinforced straight and curved ballast embankments

Computers and Geotechnics, 2018; 102:53-65

Final publication at http://dx.doi.org/10.1016/j.compgeo.2018.05.011

Three-dimensional modeling of geocell-reinforced straight and curved ballast embankments

Yang Liu, An Deng [*], Mark Jaksa

[a] School of Civil, Environmental and Mining Engineering, The University of Adelaide, SA 5005, Australia.

[*] Corresponding author.

E-mail address: an.deng@adelaide.edu.au (An Deng)

ABSTRACT

This paper outlines a three-dimensional modeling study conducted on straight and curved geocell-reinforced embankments. The study uses the discrete element method to represent varying angularities of ballast infill and models their mechanical response under monotonic and cyclic loading conditions. The simulation results show good agreement with test results and the case studies indicate that the geocell enhances embankment stiffness under monotonic loading and improves its resilience when subjected to cyclic loading. The geocell more evenly distributes stresses within the ballast embankments. The reinforced ballast embankments also exhibit less vertical displacement and lateral spreading than the unreinforced ballast embankments do.

Keywords: discrete element, railway embankment, ballast, geocell, cyclic.

1. INTRODUCTION

As time progresses, trains travel faster, railways become longer and convey heavier goods, and more stringent safety standards mandate a higher level of below-rail alignment for longer design periods. However, the main below-rail ballast layer, which is referred to in the present study as the ballast embankment, eventually becomes misaligned due to ballast breakage and rearrangement [1-4]. As a result, the embankment is prone to subsidence and lateral spreading, which undermines the safety of the tracks. The damage to the embankment is more pronounced on sharp track curves where the train creates large centrifugal forces, which can result in significant settlement in the track embankment, which exacerbates rail misalignment. Poor track geometry results in significant expenditure due to ballast inspection, maintenance and sometimes reconstruction. For example, in the year ending 30 June 2016, the Australian Rail Track Corporation (ARTC) – one of Australia's largest rail network owners – expended more than $AUD188 million on railway infrastructures maintenance work, accounting for 22.3% of their total revenue in the same year [5]. To minimize this expenditure, studies [6-9] have successfully applied geosynthetics to reinforce embankments. Of the suite of available geosynthetics, geocells provide a promising means to reinforce railway embankments [7, 8].

The geocell, as shown in Fig. 1, is a cellular confinement system developed to reinforce granular infills. The system is supplied in a folded form and, when in use, outstretched into a honeycomb-like, three-dimensional (3D) panel. The stretched panel provides a space to accommodate and confine the infill materials and facilitates the joining of individual cell panels into an integrated mattress. When fully outstretched, the panel usually measures a couple of meters in width and up to 20 meters in length, with an individual cell space of around 250 mm square, in width, and between 75 to 200 mm deep. The panel size and the cell space can be varied as part of the manufacturing process to suit individual requirements. The cell wall, which is around 5 mm thick, commonly consists of high-density polyethylene (HDPE) or other polymer material, and is perforated to allow water drainage, facilitate root growth between cells and provide interlocking with the infill.

Geocell panels have been widely used in a variety of infrastructures, such as foundations and subbases [10-16], slopes [17], retaining structures [18] and embankments [19, 20]. All of these studies have shown that using geocells improves performance of the infrastructures by reinforcing the granular infill materials. More recently, Leshchinsky and Ling [7, 8] conducted a prototype test and a finite element (FE) analysis on a geocell-reinforced railway embankment. Their studies confirmed the superiority of the geocell in reinforcing the embankment. Similar approaches were attempted in other studies [21-23]. In parallel with the FE method, Liu *et al.* [24] employed the discrete element method (DEM) to examine the performance of straight, geocell-reinforced embankments. As a further step, this study extends the DEM approach to curved embankments. Additional work includes the advanced contact model used to simulate the geocell and the examination on geocell embedment depth.

The DEM possesses the capability to represent, with appropriate engineering accuracy, distinct ballast particles and to simulate particle motion [25]. The method does not rely on a constitutive model for continuum media; rather, it incorporates a contact model developed between the individual particles. The method is also able to replicate variable angularities of the ballast, and similarly reflects variable material micro-properties, such as stiffness and friction [6, 26, 27]. More importantly, it enables 3D modeling. This is particularly important for the accurate simulation of the 3D geocell panel, as 2D modeling neglects, or at least simplifies, the interaction between cells and so underestimates the performance of the geocell panel. However, an additional calibration stage is required in order to yield simulated behavior substantially similar to that observed in reality. Further, it is not possible to simulate a full-scale structure as replacing a continuum with particle assemblies is computationally intensive. Thus, the simulation of a full-scale railway structure in DEM is beyond current computational capacity and the scope of this study.

This study adopts the commercially-available DEM program, Particle Flow Code in 3 Dimensions (PFC3D) version 4.0 [28], to simulate a geocell-reinforced embankment. The railway embankment examples included in the paper are established in accordance with the relevant codes of practice, which are discussed later. The paper aims to establish a DEM-based framework for modeling railway ballast and to evaluate the performance of incorporating geocells in ballasted embankments. Chen *et al.* [6] adopted DEM to simulate geogrid-reinforced railway ballast and they successfully demonstrated the capability of using DEM in modeling geosynthetics-reinforced ballast. The methodologies used in [6], such as material generation, have inspired the framework proposed in the current study. Improvements have also been made in the geometric complexity of ballast model as well as in the behaviors and contact models of geocell and ballast in DEM.

2. MODEL DEVELOPMENT

This section outlines the development of the ballast-geocell model in PFC3D and provides details of the particle contact and the calibration of the geocell and ballast assemblage.

2.1 Particle contact

DEM simulation is governed by the physical contact between particles. The contacts are present as a combination, in series and/or parallel, of the following basic physical elements: a bond, slider, spring and dashpot. When applying an external force to an assemblage of particles, the contacts between them determine how individual particles will respond and where they will travel at each time step in the simulation. PFC3D incorporates the contact mechanism and allows the user to encode a material-oriented, contact, constitutive model. Once validated, the model is implemented to reproduce the mechanical response of the material used in any desirable field application. The model usually defines a set of material micro-properties, such as particle stiffness, bond strength and friction coefficient, which are determined through material calibration tests.

2.2 Material calibration

In this section the procedures for calibrating the input parameters for the geocell and railway ballast in PFC3D are discussed.

2.2.1 Geocell

The geocell material was calibrated by conducting a tensile strength test. The test setup is shown in Fig. 2. A geocell strip was cut from a full panel and cropped into a standard specimen shape for tensile strength testing, in accordance with AS 1145.3 [29]. The specimen was tested using an Instron mechanical device [Fig. 2(a)] and three replicates, as the one illustrated in Fig. 2(a), were tested to obtain representative results. The stress–displacement relationship of the averaged results was then compared with the DEM simulation. The DEM simulation involved discretizing the specimen strip into 32 equal-sized spheres – an object in PFC3D for modeling materials [26]. The 32 spheres are arranged in two columns, forming a strip [Fig. 2 (b) and (c)]. Each sphere is assigned an equivalent diameter of 5 mm, and so the sphere-based strip (5 mm thick × 10 mm wide × 80 mm long) is equal in size to the specimen section, which is elongated during the test.

Table 1 shows the material micro-properties used to simulate the behavior of the geocell. The properties were determined using the formulation proposed by

Potyondy and Cundall [30] and the stress–displacement results presented in Fig. 3. As can be seen, close agreement is obtained between the simulation and test results. Both sets of results show a very close peak strength, a clear elongation process and similar residual strength. The agreement was achieved by encoding a ductile model [26] to provide a softening slope. A previous study [24] used conventional linear parallel-bond which can only provide a linear-elastic stress-strain response before reaching peak tensile strength. The ductile model is a modification, rather than a replacement to the contact-bond, and it is invoked when brittle failure occurs in bonded particles, so that the geocell model does not experience sudden failure when it reaches its peak tensile strength. Instead, the bond reduces its strength to behave like HDPE; the material from which the geocells used in this study are manufactured from. As can also be observed, there is a disparity between the simulation and experimental results in the elastic regions. This phenomenon can be attributed to the nature of the parallel-bond, which is essentially designed to model linear-elastic behavior. The model incorporates three contacts: stiffness (i.e. springs), a parallel bond and a slip. As a further note, the micro-properties shown in Table 1 were attained using an iterative approach – harmonizing the simulations with the test results [26]. Whilst this approach is somewhat indirect, satisfactory outcomes are obtained. The geocell model obtained a yielding strain ε_y=11.02% and a failure strain ε_f=46.7%; identified as points A and B respectively in Fig. 3.

2.2.2 Ballast

Railway ballast is usually produced by blasting and/or fragmenting a rock mass, and hence exhibits variable angularities. Past studies [3, 31, 32] have demonstrated the importance of accurately modeling the particle angularities, and suggested that reflecting angularities in simulations better reproduces the actual behavior of the ballast. To achieve this, four 'clump templates' were developed: trapozoidal, triangular, rectangular and hexagonal (Table 2), which account for the major geometric shapes of ballast infills. Clumps are groups of 'slaved' spheres that are firmly bonded together. In the modeling undertaken in the present study, debonding within the clump is prohibited, so as to focus on the motion of the ballast and eliminate the possibility of problems associated with breakage.

The calibration of the ballast is similar in concept to that of the geocell. Lim and McDowell [32] suggested the use of a triaxial test simulation to calibrate the ballast in PFC3D, and test results by Indraratna *et al*. [4] were used for this purpose. As suggested by Lim and McDowell [32] and Lu and McDowell [33], the interlocking of the clumps was represented by applying a weak and breakable parallel bond between two contacting clumps. The bond can reconstitutes at a new contact if particles rearrange. In addition, the membrane used to confine a sample is represented as a wall and assumed to be frictionless [6]. As PFC adopts the lower friction coefficient of two contacting entities, the friction between the clumps and the membrane is ignored. This approach is also adopted in subsequent ballast embankment models, which helps focus on the mechanical response of the geocell-reinforced ballast. Similarly, the sleepers situated on the top of the embankment act merely as loading platens and the friction between the sleepers and the ballast is ignored.

The test setup, as shown in Fig. 4, comprises a cylindrical cell of 300 mm in diameter x 600 mm high. The cell is initially filled with a number of spheres of varying diameters, 20 mm to 50 mm [Fig. 4(a)], in accordance with the ballast grading characteristics specified by Indraratna *et al*. [4]. The spheres are then replaced [Fig. 4(b)], in equal volume, with the clump templates shown in Table 2. The replacement is conducted in equal allocations among the four templates, and at random orientations within the cell. It is important to note that particle overlap occurs when assigning the clump templates to the spheres due to the created clump angularities. To negate this effect, as well as a prestressing problem, the top cap of the cell is allowed to move upward at an extremely slow rate of 0.1 mm/s until an equilibrium of inter-clump contact forces is achieved [32]. The equilibrium is determined by the ratio of the average mechanical solve ratio, defined as unbalanced force over the average value of the sum of contact forces, body forces and applied forces over all particles. The ratio is set as 1×10^{-3}, which is small enough to signal the equilibrium. The specimen porosity at equilibrium is 0.39, which is the average measured by two spheres. The spheres, 300 mm diameter each, are inscribed in the triaxial chamber. The spheres sit edge-to-edge, enabling the most occupation of the chamber space. The inscribing avoids possible boundary effect of the chamber. A total of 632 clumps (i.e. 7,584 spheres) are incorporated in the specimen.

The specimens are then subjected to triaxial compression tests at 6 different confining pressures: 15, 30, 60, 90, 120 and 240 kPa. The loading is achieved by moving top wall downward at a rate of 0.045 mm/s and the tests continue until an axial strain of 20% is attained. It should be noted that all loading rates used in this study have been selected by trial and error to achieve desirable numerical stability while reasonable computational effort is spent. A numerical, servo-control algorithm [26] is incorporated in the simulation to maintain a constant confining pressure throughout the respective loading phases. The top loading wall is assigned with following micro-properties: a normal stiffness of 1×10^{10} N/m; shear stiffness of 1×10^{10} N/m and a friction coefficient of 0.5 (i.e. tan 27°). The wall stiffnesses are higher than the ballast stiffness in order to prevent ballast penetration. Fig. 5 shows the simulation and test results of the triaxial tests. The simulation was achieved by encoding a linear contact model [26] and using the micro-properties provided in Table 3, which were obtained through trial and error. The micro-properties show that the model, similar to that for the geocell, also incorporates the three contacts: stiffness, a parallel bond and a slip. Similarly close agreement is found across the entire series of confining pressures. The accuracy of the simulations is further validated by the dilation observed under lower confining pressures and contraction under higher ones. These results demonstrate that the material properties and encoded models are capable of appropriately modeling the mechanical behavior of the ballast.

3. MODELING PROCEDURE

A full-scale embankment simulation is computationally, extremely time-consuming, owing to the large number of spheres needed to simulate the geocell and ballast infills, and is beyond current and available computer capability. This concern has been confirmed in a similar simulation study [6]. Therefore, the embankment is scaled down by a factor of five in terms of its crest and base width with regards to the actual dimensions specified by ARTC [34, 35]. In this context, there are still approximately 78,000 spheres incorporated in the reinforced embankment. The scaling does not significantly influence performance comparison made between the reinforced and unreinforced embankments, as both embankments are subject to the same level of scaling. Moreover, the scaled embankment is comparable in size with the one adopted in a prototype test [7] and so provides an opportunity to validate the simulation results against those from the test. In order to focus on the contribution of the geocell to embankment stability, a simplified track assemblage is adopted, where only sleepers are included in the DEM model and rails, fastenings and anchors are excluded.

3.1 Straight embankment

The straight rail embankment is summarized in Fig. 6. A crest width of 500 mm, base width of 1,080 mm, height of 300 mm and a length of 1,000 mm are adopted. The gradient of its shoulder slope is approximately 1:1. Six sleepers, each 50 mm wide and 500 mm long, are founded on the crest at an edge-to-edge spacing of 120 mm. The sleepers were simulated using stiff walls – an object in PFC3D for materials with line segments [26], which exhibit dimensions of actual, heavy-duty, prestressed concrete sleepers. As the contact forces between two contacting objects are governed by their stiffnesses, the sleepers are assigned with the micro-properties used for the loading wall in the triaxial simulation, enabling a consistent stress–strain behavior of the ballast assembly. Considering the 2D nature of the embankment (i.e. no longitudinal movement of the infill), the front and rear cross-sections were simulated using non-movable walls, with normal and shear stiffnesses of 1×10^{10} N/m, and a higher friction coefficient of 1.0 (i.e. tan 45°) to reflect the ballast-to-ballast friction along the section boundaries. In order to reflect embankment subsidence caused by the underlying subgrade, the subgrade was also represented by a wall, with lower normal and shear stiffnesses of 1×10^{8} N/m, and a friction coefficient of 0.5.

The role of the geocell in the stability of rail embankments is examined by placing the geocell at two different levels within the ballast layer: at the base of the embankment [Fig. 7(a)] and 50 mm above the base [Fig. 7(b)]. At each level, as shown in Fig. 7(c), the geocell panel is centered within the ballast-filled embankment. The panel [Fig. 7(d)] includes 8 cells and measures 748 mm × 480 mm edge-to-edge. Each cell is 75 mm deep and 175 mm × 175 mm wide. The long and short sides of the panel are aligned with the embankment's longitudinal and transverse directions, respectively. The short side is less than the width of embankment crest, so that a 10 mm margin is present along the embankment crest edges. In the longitudinal direction, the panel length is 252 mm shorter than the extension of the embankment, which negates boundary effects associated with the panel. The geocell panel is longitudinally divided into two halves: *A* and *B*. Representative cell junctions are marked as *a* to *g* for subsequent displacement analysis. As is required by PFC3D, the geocell material is also simulated by a layer of spheres. The spheres are aligned and bonded together contiguously using the micro-properties shown previously in Table 1. A total of 12,762 spheres are used to generate the entire geocell panel.

The ballast infill is generated using the procedures similar to those used in the ballast triaxial calibration. Temporary walls are generated first on the embankment slopes and crest as boundaries. The geocell and associated bonds are then generated within the pre-defined boundaries, followed by generation of ballast and corresponding parallel-bond. The geocell can deform freely and it is breakable during this process. It should be noted that the ballast is generated in three layers (i.e. 100 mm thick each). As contact forces between clumps are created due to overlapping during clumps generation, additional time steps are permitted between the generations of each layer, so that previous layers can reach equilibrium (i.e. release contact forces). The temporary walls prevent the escape of clumps due to the contact forces and they are permitted to move slowly outward until the inter-clump contact forces dissipate, upon which they are removed. During the ballast generation process, no constraint is applied to the interaction between the geocell and ballast. This is to reflect the actual placement of ballast in the field. A total of 4,002 clumps (i.e. 56,083 spheres) are used for the infill in the situations where a geocell panel is used. For the unreinforced embankment, similar numbers of clumps (4,106) and spheres (57,479) are generated for the infill.

3.2 Curved embankment

A horizontally-curved embankment has its outer rail elevated to provide a banked curvature. This super-elevation, also known as a cant, serves the purpose of providing a centripetal force to balance the centrifugal force exerted by the train's motion, which in turn allows the train to negotiate bends at higher speed. Fig. 8 shows a diagram of the curved embankment used in this study. The diagram is similar to that for the straight embankment except for the 5% gradient adopted at the crest. This gradient is set in accordance with ARTC [35] and the value corresponds to the typical limit of super-elevation for an intrastate line in Australia. Compared with the straight embankment, the curved embankment uses the same geocell arrangements and material micro-properties, and a similar number of spheres for the geocell and ballast.

3.3 Monotonic and cyclic loading

This sub-section describes the monotonic and cyclic loading adopted in the study. The aim of the monotonic loading is to determine the embankment subsidence in response to a slowly increasing vertical load and is similar in nature to a plate load test. For the straight embankment, the numerical model constrains the sleepers to move in a downward direction along a trajectory normal to the crest. The sleepers advance at a rate of 0.1 mm/s to cause the embankment to settle at the desired strain of 20% (60 mm). The modest value of the loading rate improves the simulation accuracy by allowing sufficient time to calculate the inter-particle contact forces. The strain-limiting value is consistent with that used in the triaxial calibration and helps predict the load extremes that the embankments can sustain. The monotonic loading applied to the curved embankment acted at an angle of inclination θ (i.e., 54.5° = arctan(P_L/P_V)) [Fig. 9], where P_V is the vertical applied load and is calculated to equal 125 kPa for a 30-tonne axle load of a heavy haul train wagon [34]; P_L is the lateral load acting on the sleepers and equal to the centrifugal force as:

$$P_L = \frac{mv^2}{R} \qquad (1)$$

where m is the axle load, v is the speed of the train, and R is the horizontal curve radius. ARTC [34] specifies R = 200 m as the minimum allowable horizontal curve radius for a heavy haul line. Thus, P_L is approximately 175 kPa when the haul train wagon passes through the curve at the ARTC's design speed of 60 km/h [36]. The values for the vertical load, radius and design speed are adopted to reflect adverse situations in practice and so amplify the loading conditions and expedite the simulation process. To achieve a displacement direction at the angle θ, the sleepers advance at a lateral rate of 0.14 mm/s and vertical rate of 0.1 mm/s; that is, at a velocity ratio of 1.4, which is equivalent to the P_L/P_V ratio.

Cyclic loading, on the other hand, is of higher significance in regard to the assessment of the long-term serviceability of railway embankments. For the straight embankment, a vertical load of P_V = 125 kPa, which reflects a full-scale 25-tonne heavy freight train passing through, was applied normal to the sleepers in the form of loading-complete unloading-reloading cycles. Although the geometry of the railway structure and geocell is downscaled, the strength and mechanical behavior are calibrated against laboratory and full-scale experimentation, therefore no scale factor is applied to the loading values. The load applied has been shown to be frequency-independent, as reported by Shenton [37]. Due to the long computational time when performing the simulation, a total of 20 loading cycles were performed for each simulation. Even with this somewhat modest number, the simulations utilized the full capability of the PC hardware (Intel core i7-4500U, 8GB DDR3L 1333 RAM with integrated Intel HD Graphics 4400) and the entire modeling process took approximately two months to complete. Albeit with the constraint of computational time, the simulations provide indicative observations of embankment subsidence and the performance of geocells in the early stages of the cyclic loading. Similar simulations were applied to the curved embankment, except for the load applied. The resultant force (P_R) of the vertical (P_V) and lateral (P_L) loads was calculated as 215 kPa and acted at an angle of θ with respect to the vertical direction (Fig. 9). It is worth mentioning that for both straight and curved embankment subject to cyclic loading cases, all sleepers advance simultaneously at the same rates. No lag is applied to the sleepers to reflect train passage as the freight can pass the sleepers gap in an extremely short period of time over a 1-meter embankment.

Local damping was activated for ballast clumps only to absorb the vibration energy generated in the cyclic loading process. The clumps tend to rebound and occasionally escape from the embankment boundaries during the unloading phases, as a result of accumulated internal forces. The introduction of a damping coefficient, ζ, facilitates the dissipation of these forces in the agitated clumps and allows the ballast assembly to cease oscillating more rapidly [26]. In this study, the local damping ratio was set to 1.0.

4. RESULTS AND DISCUSSION

4.1 Straight embankment

Fig. 10 shows the vertical displacement of the sleepers plotted against the applied vertical load for the straight embankments under monotonic loading, where the results of the numerical simulations from this study are compared with the test results presented by Leshchinsky and Ling [7]. The simulated vertical displacement is the average of the 6 sleepers and the load is the average resistance measured at the base of the sleepers [Fig. 6(b)]. The boundary effects caused by the walls in longitudinal direction are neglected in this study as the individual data set for each sleeper shows insignificant differences in axial stress value. Unlike traditional FE analysis, the results of the DEM modeling show a somewhat irregular curve with slight fluctuations. These are associated with the rearrangement of clumps as the applied load increases. Overall, the vertical displacement rises with increased load for the three design cases, without defined yielding for the range of loads applied. It is clear that using a geocell panel has a noticeable influence on the vertical displacement of the embankment. With the same applied load, the geocell-reinforced embankment exhibits less vertical displacement than that of the unreinforced embankment. Specifically, given a load of 125 kPa, the vertical embankment displacements are 18.9 mm, when the geocell is located 50 mm above the base, 27.9 mm when the geocell is founded at the base, and 29.5 mm when the embankment is unreinforced. As shown in Fig. 10, the performance of the geocell reinforcement is in agreement with the test results presented by Leshchinsky and Ling [7], who conducted a similar monotonic loading test on a geocell-reinforced ballast embankment. This implies that incorporating a geocell panel in a railway embankment will reduce vertical displacement, and placing it 50 mm above the base, yields superior performance to that when the geocell is placed at the base. The superiority can be attributed to the position of geocell. The suspended geocell limits the loading propagating into the bottom 50 mm layer, which minimizes the settlement and lateral spreading of the bottom layer.

The monotonic loading curves, given in Fig. 10, can be subdivided into two zones: *A* and *B*, which correspond, respectively, to vertical displacements of less than 10 mm and those beyond 10 mm. In Zone *A,* the early stages of vertical embankment displacement, the sleepers displace in a similar fashion across the three cases examined and exhibit largely equal stiffness. This implies that the ballast skeleton supports the majority of the load when the load remains at a relatively low level, and the geocell is ‘at rest’ and contributes little to the embankment stiffness. In Zone *B*, where the vertical displacement exceeds 10 mm, the geocell demonstrates a strain-hardening effect. It aids in reinforcing the ballast skeleton and increases the stiffness of the embankment. As a result, for an equal vertical displacement, the geocell-reinforced embankment is able to support a higher load than the unreinforced embankment. Due to the curves fluctuation, however, there is a section disagreeing the comparison. Where the vertical load falls into 165 to 220 kPa, the reinforced embankment with geocell at base experiences slightly higher vertical displacement than the unreinforced does, with a maximum difference of 2.3 mm. The curves fluctuation is caused by the DE simulation attaining convergence at some time steps. In addition, placing a geocell 50 mm above the base provides an improved stiffness response than placing it at the base.

Fig. 10 also presents a comparison of the stiffness development between the simulation results and the prototype test results presented by Leshchinsky and Ling [7] who placed geocell at 100 mm above base. The inclusion of this set of experimental data is not for making quantitative comparison against the results obtained from this study (place geocell at 50 mm above base). The intention is to claim that by suspending geocell within ballast embankment, further improvements can be made, and it has been validated by previous experimentation. As can be seen, both sets of results show a short segment of low stiffness, in the early stages of monotonic loading, followed by a more prolonged development of improved stiffness. Once the results enter Zone *B*, placing geocell at 100 mm above the base becomes more advantageous in reducing sleeper’s displacement than placing geocell at 50 mm does. The displacement difference is up to 5.2 mm when the vertical load reaches 285 kPa. From this point onward, the reinforcing effect decreases and the two curves cross over where the vertical load increases to 498 kPa. Afterward, placing geocell at 50 mm offers better performance until the end of simulation. Overall, both studies indicate that suspending geocell within the ballast embankment can yield better load-bearing performance. This agreement, however, is not observed with the unreinforced embankments. Strain-softening was observed in the test embankment, whereas the simulated embankment exhibits strain-hardening throughout. Therefore, the unreinforced test embankment yields a lower secant stiffness than in the simulation: 2,916 kPa/m for the test and 7,975 kPa/m for the simulation, at a vertical displacement of 60 mm.

This disagreement arises mainly from the unconfined nature (in both longitudinal and transverse directions of the embankment) of the prototypical test conducted by Leshchinsky and Ling [7]. The ballast can move freely in both directions, whereas the longitudinal movement is prohibited in the current models by installing two boundary walls. In addition, the difference between the test and simulated ballast infill, as well as other factors such as embankment geometry, loading plate size, geocell strength and boundary conditions, may also contribute to the significant difference in vertical displacement. The gravel that was used in the test is smaller on average than the ballast used in the simulation (D_{50} = 15.5 mm and 35 mm, respectively) and so yields a lower shear strength. This is confirmed by the respective triaxial test results; for example, a shear strength of approximately 400 kPa for the gravel in the test [7] and 700 kPa for the coarser aggregate in the simulation, when subjected to the same confining pressure of 90 kPa. The lower shear strength for the gravel leads to its strain-softening behavior and lower stiffness. It is interesting to note that the discrepancy occurred with the unreinforced embankment, whose behavior is dissimilar to that of the reinforced embankment. This implies that the use of a geocell panel is able to mitigate potentially 'weak' properties of the ballast infill and increase stiffness through its reinforcement effects.

Fig. 11 shows sleeper's vertical displacement plotted against the number of load cycles for the straight embankment under cyclic loading. It is evident that the geocell is effective in reducing vertical displacement associated with cyclic loading. During the initial 5 loading cycles (Zone *A*), all three cases exhibit a high displacement rate. Similar behavior is observed in a previous study [6] where geogrid is used. The early-stage quick displacement also agrees with the results obtained by Selig and Waters [38] who found that the relatively rapid displacement in the early stage is associated with the poorly consolidated nature of infills. In Zone *A*, the vertical displacement is reduced due to the use of geocell. However, no noticeable difference is observed between placing geocell at base and 50 mm above the base. The role of geocell becomes more pronounced as the cycle number increases which is suggested by the noticeably slower displacement rates in Zone *B* (5^{th} to 20^{th} loading cycle). This phenomenon can be attributed to the passive-confinement mechanism of geocell. Where cyclic loading continues, the infills is further compacted, stiffening the geocell mattress, which in turn provides better reinforcement to the ballast embankment. In Zone *B*, placing geocell at 50 mm above base outperforms placing geocell at base. The reinforcing effect improves slightly along with the increase of load cycle number, resulting in a final vertical displacement of 45.5 mm versus 52.3 mm if placing geocell at base. Interestingly, Chen *et al.* [6] who installed geogrid in ballast embankment as reinforcement at 50, 100 and 150 mm concluded otherwise. Their study reported that placing geogrid at lower levels (i.e. 50 mm above subgrade) better prevents the displacement. There is no clear reason to this disagreement, but the two geosynthetic materials work in different modes: cell confinement by the geocell and grid-particle friction by the geogrid. It is suggested that the confinement matter works better if placed next to the load on ground; the geogrid is placed at a lower level where the load becomes spread and reduced.

Comparison to the past study [7] has been made in the final vertical displacement only as the original displacement versus loading cycle relationship is unavailable. After the 20th cycle, the simulations show higher vertical displacement than that indicated by tests. The vertical displacement is 67.5 mm for the simulation and approximately 48 mm for the unreinforced embankment test; and 52.3 mm when placing geocell at 50 mm above base for the simulation and approximately 31 mm for the test of the embankment incorporating the geocell at the 100 mm above base. In addition to the compaction effort, other factors that may contribute to the final settlement difference are the size effect at the plate-infill interface and the geocell types used. The simulations use a sleeper of 50 mm × 500 mm and infill of D_{50} = 35 mm, and the test used a square plate, 356 mm × 356 mm in size, and infill of D_{50} = 15.5 mm. The smaller sleeper-infill size ratio for the simulations results in the sleepers ‘punching’ to a greater extent into the infill than the test does. This punching effect likely reduces with depth as the lateral resistance (arching) of the infill between neighboring sleepers increases, and the displacement stabilizes. On the other hand, Leshchinsky and Ling [7] adopted Novel Polymetric Alloy (NPA) geocell which exhibits higher stiffness and tensile strength (27 MPa) than typical HDPE geocell [14, 31]. The material strength difference can also prevent embankment settlement.

In order to gain a greater insight into the force distribution and transmission mechanism of unreinforced and reinforced ballast embankments, as shown in Fig. 12, contact forces are drawn at the same scale for the straight embankments after the 20th cycle. The contact forces are observed through the front cross section of the respective embankments. It can be seen that the contact forces develop in different patterns between the unreinforced and reinforced embankments. The unreinforced embankment shows an uneven distribution of contact forces. The forces adjacent to the base of the embankment are more concentrated than elsewhere in the embankment. In contrast, the contact forces for the geocell-reinforced embankments are distributed more evenly. This even distribution of contact forces helps eliminate overstressing of the infill and reduces the likelihood of localized displacement and/or failure, thus improving the resilience of the embankment. In addition, an increase in the maximum and average contact forces within the ballast are recorded among the three cases simulated. The unreinforced case exhibits the lowest contact force value comparing to the two reinforced cases. This difference can be attributed to the higher internal contact forces induced by a reduced settlement. The internal stress caused by loading cannot dissipate through particle movement as it is restricted by the geocell panel. The highest contact force is observed where the geocell panel is placed 50 mm above the base, which implies less ballast movement should be expected. This observation agrees with results shown in Fig. 10 (monotonic loading case). That is, at the same settlement, the reinforced cases sustain loads greater than the unreinforced case does.

Fig. 13 shows the total particle displacement vectors (i.e. the combination of vertical and lateral displacement) of the ballast after the 20th cycle, again drawn at the same scale as that shown previously to allow visualization of the microstructure strain evolution of the embankments. Fig. 13 (c) is tilted by 5 degrees for better visualization of the displacement vectors, which causes the vectors appear slightly denser and longer. Apart from the reduced particle displacement, the major difference between the unreinforced and the reinforced embankments lies in the direction of the ballast displacement. The infill in the reinforced embankments [Fig. 13 (b and c)] displace mainly toward the base, whereas the infill in the unreinforced embankment [Fig. 13 (a)] tends to move laterally. This can be better visualized in Fig. 13 (d-f) which provide zoomed-in views of the left-hand-side unreinforced sections of three embankments. These observations confirm the ability of the geocell panel to prevent the ballast infill from spreading That is, the geocell panel helps restrain the confined infill equivalent to that of a relatively rigid pad. In this way, the pad effectively absorbs overlying loads and transfers them downward, avoiding or reducing lateral spreading. This is consistent with the distribution of contact forces shown previously in Fig. 12(b and c), where the contact force concentration is less significant at the base of the embankments and thus reduces embankment displacement. The central part of the elevated geocell panel [Fig. 13 (c)] undergoes modest subsidence (approximately 10 mm), which suggests slight lateral movement of the infill underlying the panel.

Fig. 14 shows the total displacement vectors for the geocell panels after the 20th loading cycle, as well as the maximum displacements and their approximate locations. These displacement vectors are scaled up by a factor of 50 in order to achieve better visualization. As can be seen, the panels undergo a limited amount of displacement and they hence remain effectively in their original configuration after repetitive loading, demonstrating their strength. In the case where the geocell is placed at the base [Fig. 14 (a)], the maximum displacement occurs at the bottom-left of the panel. This location shifts upward when the panel is located 50 mm above the base. The relocation implies that the geocell panel settles noticeably (10 mm approximately) together with the ballast assembly. In addition, the displacement is not position-dependent. All cell walls, at the center and along the edges, undergo a similar level of deformation. This behavior aids in evening out the stresses acting on the panel, eliminating local failures, maintaining its long-term reinforcement capability and, more importantly, accommodating the displacement of the infill and harmonizing the particle contact forces.

4.2 Curved embankment

The vertical and horizontal displacements plotted against the corresponding loads of the curved embankment that was subjected to the resultant load, P_R, (Fig. 9) are shown in Fig. 15. The load-vertical displacement curves [Fig. 15(a)] develop in a form similar to those observed with the straight embankment [Fig. 10]. Non-yielding is clearly evident upon the load of 600 kPa. The three curves exhibit largely equal stiffness when the displacement is low (i.e. less than 10 mm), where the vertical displacement mainly arises from rearrangement of the uncrushable infill (in the DEM model, in any case) and the geocell provides a marginal contribution to stiffness. The geocell's reinforcement effect becomes clear when the displacement exceeds 10 mm. It can be seen that the geocell-reinforced embankments obtain stiffness higher than that of the unreinforced embankment, and so support a greater load, given the same vertical displacement. Placing the geocell 50 mm above the base yields a higher stiffness. Similar improvement occurs in the lateral direction [Fig. 15(b)], where the sleepers of the reinforced embankments displace less than the sleepers of the unreinforced embankment, with an equal resultant load. This is attributed to the geocell enhancing the interlocking of the infill and so restraining the rearrangement and rotation of the ballast particles. In the later stages of loading (i.e. > 40 mm lateral displacement), lateral yielding occurs in all simulations, showing a marked displacement in response to the cyclic loading. This is a result of the sleepers having partially moved out of the region influenced by the geocell, and thus having to rely on the shoulder ballast to provide lateral resistance. This observation is valid for all simulations performed for curved embankments. Although this phenomenon is unlikely to occur in actual railways, as catastrophic accidents can be caused due to de-railing, the results are presented for the purpose of demonstrating the improvements derived from placing geocell in railway ballast embankments.

Fig. 16 shows the vertical and lateral displacement of the sleepers due to cyclic loading. As was evident with monotonic loading, the geocell-reinforced embankments outperform the unreinforced embankment. The reinforced embankments exhibit less vertical and lateral displacements than those observed in the unreinforced embankment. Placing a geocell 50 mm above the base, again, better controls displacement in both the vertical and horizontal directions. The vertical displacement [Fig. 16(a)] is more pronounced over the first 5 cycles, and then shows a decreased rate over the remaining cycles. The lateral displacement of the sleepers is relatively high, given the low number of cycles [Fig. 16(b)]. This is likely caused by the unrestrained nature of the sleepers, where the restraining influence of the track structure, such as the rails, rail anchors and fastenings, were not taken into account in the simulations, as mentioned earlier. As a result, the sleepers are able to displace more freely than would occur in the field.

Fig. 17 shows the inter-particle contact forces drawn at the same scale after the 20th load cycle. As for the straight embankments, the geocell panels also appear to promote an even stress distribution for the curved embankments. This is in agreement with the particle displacement vectors shown in Fig. 18, where reduced spreading is observed for the reinforced embankments, when compared with the unreinforced embankment. Moreover, comparing the displacement vectors with those for the straight embankments (Fig. 12) implies that the geocell panels in the curved embankments are similarly effective in forming a relatively rigid platform and to mitigate ballast spreading.

Fig. 19 shows the total displacement vectors for the geocell panels after the 20th cycle. The panels maintain their respective initial shape and demonstrate the geocell's capability to sustain the lateral load for the curved embankments. The geocell walls, in particular the walls adjacent to the longitudinal centerlines, deflect to the right – in line with the direction of the resultant forces. The concurrent deflection of the walls helps counteract the lateral load, confine the lateral load within the area of the panel, and reduce spreading of the infill along the edges. The panel situated 50 mm above the base appears to deflect slightly more than does the panel at the base. This is consistent with the geometric deformation which occurs in a 'suspended' panel [Fig. 18 (c)], and suggests it is likely to degrade sooner than the panel located at the base. This can be examined through additional case studies, such as increasing load cycles and placing panels at higher levels in the embankment. This is, however, beyond the scope of the present paper.

To gain a further insight into the deflection of the geocell panel, geocell strains are captured. As illustrated in Figure 20, for a pair of neighboring spheres of interest, the strain, ε, is defined as the edge-to-edge distance after displacement, D_1–D_0, to the initial center-to-center distance, D_0. The strain values at locations of interest are summarized in Table 4. These include junctions *a* to *g*, panel halves *A* and *B*, as shown in Fig. 7(d), and locations of maximum strain for the geocell panels at the base and 50 mm above the base, subjected to the monotonic and cyclic loading scenarios. Panel halves *A* and *B* rest on the lower and the higher side of the embankment, respectively.

The initial center-to-center distance is 5 mm, as shown in Fig. 2(b). The strain at a junction is calculated as the average strain of all spheres within 20 mm (i.e. 11.4% of the cell side) to the junction. The selected percentage is intended to reflect the strain in the proximity of the junction. The strain for either half panel is the average strain of all the spheres belonging to that half panel. The strain values in Table 4 show that the geocell deforms at every junction with varying magnitude, for instance, ranging from 24.1% to 41.6% for the geocell at the base when subjected to monotonic loading. Where the sleepers advance less under the cyclic loading, noticeably lower strains of 14.1% on average occur to the junctions. There is a clear difference in strain between the panel halves *A* and *B*, where all other design details remain the same. For instance, the average strain is 18.5% for panel half *A* and 24.9% for panel half *B* under monotonic loading. This implies that greater deflection occurs at the part of the geocell that provides direct reaction to the inclined train load P_R. Lower strains occur to both halves where the geocell is placed 50 mm above the base than the geocell placed at the base, which agrees with the embankment displacement results shown in Figs. 11 and 16. Under the monotonic loading, the entire panel is subject to a maximum strain of 39.7%, if placed at the base, and 45.6%, when placed 50 mm above. If subjected to the cyclic loading, the panel shows a maximum strain of 28.4%, when at the base, and 23.4%, when 50 mm above. The magnitude of these strains indicates that the geocell panel remains at the pre-failure state for the load levels simulated. The approximate locations, L1 to L4, where maximum strains were recorded, are highlighted in Figure 21; i.e. L1 for 39.7% and L2 for 45.6% under the monotonic loading scenario, and L3 for 28.4% and L4 for 23.4% under the cyclic loading scenario. There is no clear pattern to the locations of maximum strain, however, as can be seen, they are all consistent with the center of a cell-wall. This indicates that cell-walls undergo greater deflection than the junctions do, as one might expect.

5. CONCLUSIONS

This study assesses the use of geocells in reinforcing railway ballast embankments. Discrete element modeling has been conducted, using clumped particles to simulate angular ballast, to evaluate bearing capacity, vertical displacement and lateral spreading of the embankment, as well as providing insights into the micro-behavior of the ballast infill and the geocell, including contact forces and displacements. Straight and curved embankments have been subjected to monotonic and cyclic loading conditions and the modeling results have been compared with previous, published test results. The conclusions of this study are as follows:

1. The simulation results for the straight, reinforced embankment are in reasonably good agreement with the test results. This suggests that the discrete element modeling is valid and is an appropriate method to assess the mechanical response of railway embankments.
2. For the unreinforced, straight embankment, however, simulation results show modest agreement with the past test results. The suboptimal agreement may be attributed to the differences in the particle size distribution, embankment geometry and loading magnitude. These factors influence the embankment performance where reinforcement is not used.
3. The presence of a geocell within the ballast stiffens both straight and curved embankments. Geocell-reinforced embankments exhibit less vertical displacement and lateral spreading compared with unreinforced embankments and so aid in maintaining a safer track alignment in the longer term. The embankments with a geocell suspended 50 mm above the base are stiffer than the embankments with a geocell located at the interface between the ballast and the subgrade. The former, however, deflects more than the latter and so risks having a reduced operational life. The geocell embedment depth results disagree with results in Chen *et al.* [6] which used geogrid to reinforce straight embankment. Their study suggests that placing geogrid at a higher level causes less vertical displacement than placing it close to the subgrade.

4. The geocell constrains the displacement of the encased ballast infill to form a relatively solid mattress. The mattress helps absorb overlying loads, increase the stiffness of the embankment, reduce spreading of the infill and balance forces in the embankment.

Whilst the study proposes a valid approach to demonstrate and examine the effects of reinforcing railway ballast with geocell, a number of limitations and assumptions were adopted to undertake successfully the DEM simulation:

1. The geocell model was calibrated solely against a series of tensile strength tests. Other properties such as puncture resistivity, flexural stiffness and torsion stiffness were not considered in the current study. Attempts will be made to incorporate these material properties in future studies to improve the reliability of the modeling framework.
2. Whilst the use of clumps provides a more accurate representation of ballast angularity, when compared with the adoption of entirely spherical particles, their shape does not fully reflect actual ballast angularities and, hence, have limited capability to simulate accurately ballast interlock and inter-particle friction. Defining the clumps as non-breakable in the simulation, may also result in overestimating the long-term performance of the embankment. It is plausible to conduct a 3D simulation of the embankment, but the scaled-down embankment may compromise the simulation accuracy.
3. In simulation, the ballast is calibrated against the monotonic test results. The calibration can possibly improve where cyclic loading test results are available and used. However, as stated in previous study [33], the

calibration against cyclic test results can be extremely time consuming. Due to this reason, this calibration step was neglected, enabling a focus on the simulation of ballast embankments.

4. Due to the limited number of load cycles applied to the embankment, the results presented may not accurately reflect the long-term performance of the ballast embankment. Along with advancement in PFC3D and computational capacity, this issue can be resolved in future studies. In addition, the number and location of inter-clump parallel-bond breakage, which can provide in-sight on the ballast re-arrangement, was not recorded. It will be taken into consideration in our future studies when ballast breakage is incorporated into the modeling framework.

Acknowledgement

The authors wish to thank Mr. Rod Fyfe from Geofabrics Australasia for his assistance in this research.

Notation

D_0	center-to-center distance of neighboring spheres, before displacement
D_1	center-to-center distance of neighboring spheres, after displacement
D_{50}	diameter of particles 50% finer by weight
k_n	normal stiffness
k_s	shear stiffness
$\bar{k}_n$	parallel-bond normal stiffness
$\bar{k}_s$	parallel-bond shear stiffness

$\hat{k}_{s}$ softening stiffness

$\hat{k}_{n}$ normal stiffness in tension

P_{L} lateral load

P_{R} resultant load

P_{V} vertical load

R track horizontal curve radius

$\overline{R}$ bond radius

v train velocity

μ friction coefficient

θ angle of inclination

ρ density

$\overline{\sigma}_{c}$ parallel-bond normal strength

$\overline{\sigma}_{t}$ tensile strength

$\overline{\tau}_{c}$ parallel-bond shear strength

ζ local damping coefficient

ε geocell strain

ε_{y} geocell yielding strain

ε_{f} geocell failure strain

References

[1] Hossain Z, Indraratna B, Darve F, Thakur PK. DEM analysis of angular ballast breakage under cyclic loading. Geomech Geoeng. 2007;2(3):175–81.

[2] Salim W, Indraratna B. A new elastoplastic constitutive model for coarse granular aggregates incorporating particle breakage. Can Geotech J. 2004;41(4):657–71.

[3] Yan Y, Zhao J, Ji S. Discrete element analysis of breakage of irregularly shaped railway ballast. Geomech Geoeng. 2014:1–9.

[4] Indraratna B, Ionewscu D, Christie HD. Shear behavior of railway ballast based on large-scale triaxial tests. J Geotech Geoenviron Eng. 1998;124(5):439–49.

[5] ARTC. Australian Rail Track Corporation 2016 Annual Report. Australia: Australian Rail Track Corporation Ltd., 2016.

[6] Chen C, McDowell GR, Thom NH. Discrete element modelling of cyclic loads of geogrid-reinforced ballast under confined and unconfined conditions. Geotext Geomembr. 2012;35: 76–86.

[7] Leshchinsky B, Ling H. Effects of geocell confinement on strength and deformation behavior of gravel. J Geotech Geoenviron Eng. 2013;139(2):340–52.

[8] Leshchinsky B, Ling HI. Numerical modeling of behavior of railway ballasted structure with geocell confinement. Geotext Geomembr. 2013;36: 33–43.

[9] Miao C-X, Zheng J-J, Zhang R-J, Cui L. DEM modeling of pullout behavior of geogrid reinforced ballast: The effect of particle shape. Comput Geotech. 2017;81:249–61.

[10] Hegde A, Sitharam TG. 3-Dimensional numerical modelling of geocell reinforced sand beds. Geotext Geomembr. 2015;43(2):171–81.

[11] Moghaddas Tafreshi SN, Shaghaghi, T., Tavakoli Mehrjardi, G., Dawson, A.R., Ghadrdan, M. A simplified method for predicting the settlement of circular footings on multi-layered geocell-reinforced non-cohesive soils. Geotext Geomembr. 2015;43:332–44.

[12] Tanyu BF, Aydilek AH, Lau AW, Edil TB, Benson CH. Laboratory evaluation of geocell-reinforced gravel subbase over poor subgrades. Geosynth Int. 2013;20(2):47–61.

[13] Dash SK. Effect of geocell type on load-carrying mechanisms of geocell-reinforced sand foundations. Int J Geomech. 2012;12(5):537–48.

[14] Yang X, Han J, Pokharel SK, Manandhar C, Parsons RL, Leshchinsky D, et al. Accelerated pavement testing of unpaved roads with geocell-reinforced sand bases. Geotext Geomembr. 2012;32:95–103.

[15] Oliaei M, Kouzegaran, S. Efficiency of cellular geosynthetics for foundation reinforcement. Geotext Geomembr. 2017;45:11–22.

[16] Dash SK, Bora MC. Improved performance of soft clay foundations using stone columns and geocell-sand mattress. Geotext Geomembr. 2013;41:26–35.

[17] Mehdipour I, Ghazavi M, Moayed RZ. Numerical study on stability analysis of geocell reinforced slopes by considering the bending effect. Geotext Geomembr. 2013;37:23–34.

[18] Chen R-H, Wu C-P, Huang F-C, Shen C-W. Numerical analysis of geocell-reinforced retaining structures. Geotext Geomembr. 2013;39:51–62.

[19] Zhang L, Zhao M, Shi C, Zhao H. Bearing capacity of geocell reinforcement in embankment engineering. Geotext Geomembr. 2010;28(5):475–82.

[20] Madhavi Latha G, Rajagopal K. Parametric finite element analyses of geocell-supported embankments. Can Geotech J. 2007;44(8):917–27.

[21] Nishiura D, Sakai H, Aikawa A, Tsuzuki S, Sakaguchi H. Novel discrete element modeling coupled with finite element method for investigating ballasted railway track dynamics. Comput Geotech. 2018;96:40–54.

[22] Xu M, Hong J, Song E. DEM study on the effect of particle breakage on the macro- and micro-behavior of rockfill sheared along different stress paths. Comput Geotech. 2017;89:113-27.

[23] Zhang L, Zhao M, Shi C, Zhao H. Nonlinear analysis of a geocell mattress on an elastic–plastic foundation. Comput Geotech. 2012;42:204–11.

[24] Liu Y, Deng A, Jaksa M. Discrete element modelling of geocell-reinforced track ballast under static and cyclic loading. Proc The 12th Australia–New Zealand Conference on Geomechanics. Wellington, New Zealand2015. p. 279–86.

[25] Cundall PA, Strack ODL. Discrete numerical model for granular assemblies. Geotechnique. 1979;29(1):41–65.

[26] Itasca. PFC3D 4.0 User's Manual. Minnesota, USA: Itasca Consulting Group, Inc., 2009.

[27] Irazábal J, Salazar F, Oñate E. Numerical modelling of granular materials with spherical discrete particles and the bounded rolling friction model. Application to railway ballast. Comput Geotech. 2017;85:220–9.

[28] Itasca. Particle Flow Code in Three Dimensions Version 4. Monnesota, USA: Itasca Consulting Group, Inc., 2009.

[29] SAI. Determination of Tensile Properties of Plastics Materials. AS 1145.3: Standards Australia International Ltd., 2001.

[30] Potyondy DO, Cundall PA. A bonded-particle model for rock. Int J Rock Mech Min. 2004;41(8):1329–64.

[31] Le Pen LM, Powrie W, Zervos A, Ahmed S, Aingaran S. Dependence of shape on particle size for a crushed rock railway ballast. Granul Matter. 2013;15(6):849–61.

[32] Lim WL, McDowell GR. Discrete element modelling of railway ballast. Granul Matter. 2005;7(1):19–29.

[33] Lu M, McDowell GR. DEM of railway ballast under monotonic and cyclic triaxial loading. Geotechnique. 2010;60(6):459-67.

[34] ARTC. Engineering (Track & Civil) Code of Practice. Section 2 Sleepers and Fastenings. Australia: Australian Rail Track Corporation Ltd., 2017.

[35] ARTC. Engineering (Track & Civil) Code of Practice. Section 5 Track Geometry. Australia: Australian Rail Track Corporation Ltd., 2016.

[36] ARTC. Route Access Standard. General Information. Australia: Australian Rail Track Corporation Ltd., 2014.

[37] Shenton MJ. Deformation of Railway Ballast Under Repeated Loading Conditions. Railroad Track Mechanics and Technology. Derby: British Railway Research and Development Division, 1978. p. 405-25.

[38] Selig ET, Waters JW. Track Geotechnology and Substructure Management. London, UK: Thomas Telford, 1994.

Figures

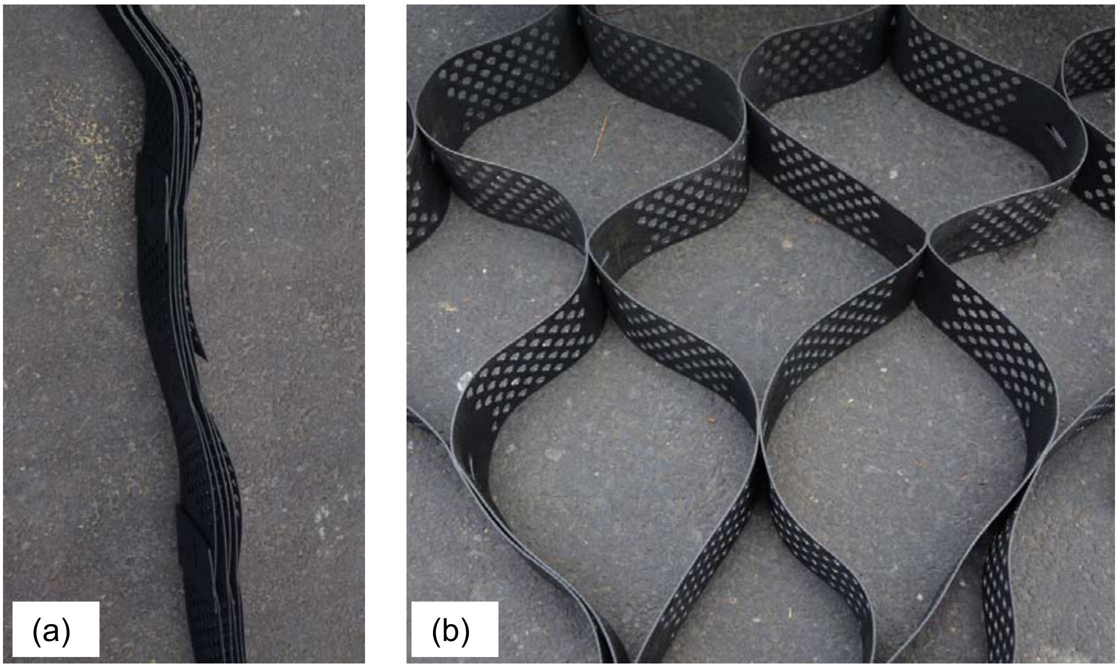

Fig. 1. Information on cell size and wall depth: (a) folded and (b) outstretched (250 $W \times 250$ $L \times 100$ D mm for a cell).

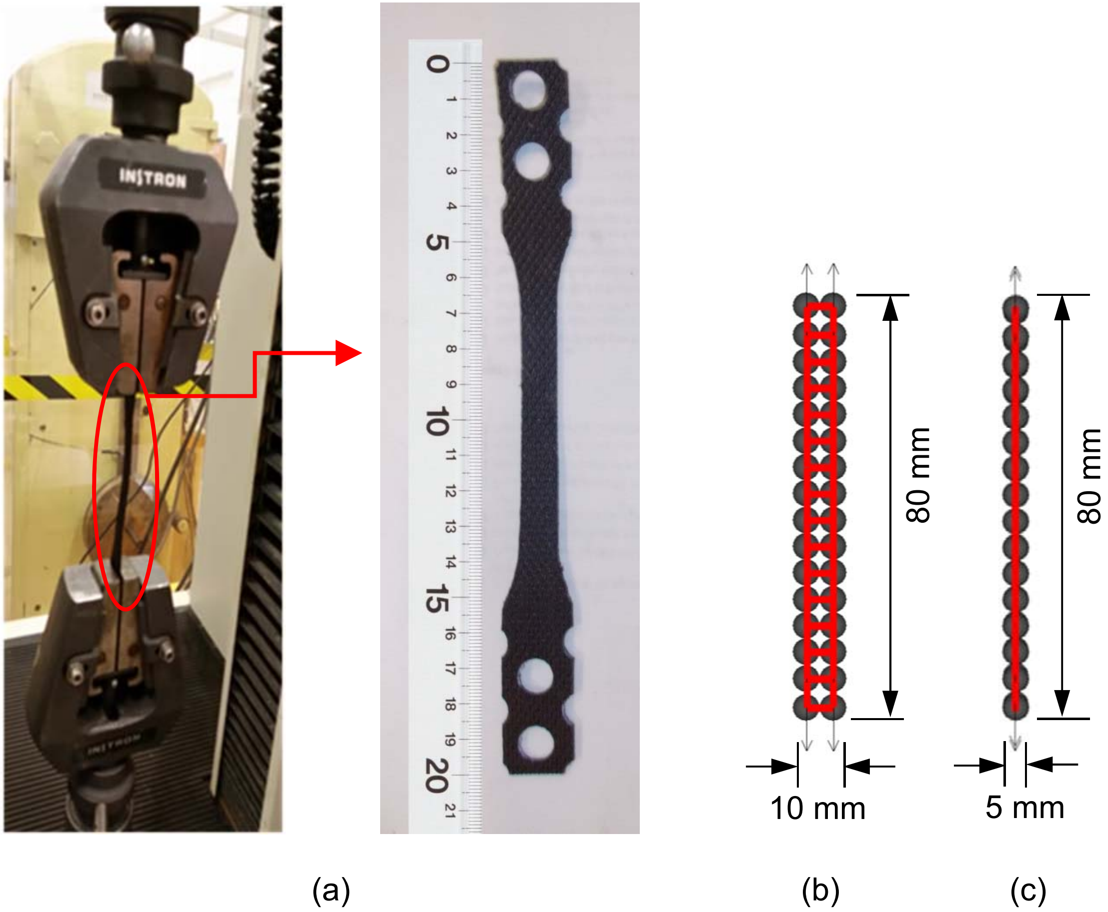

Fig. 2. Geocell tensile strength test: (a) setup and detail of representative tested specimen; (b) front view in DE simulation; (c) side view in DE simulation.

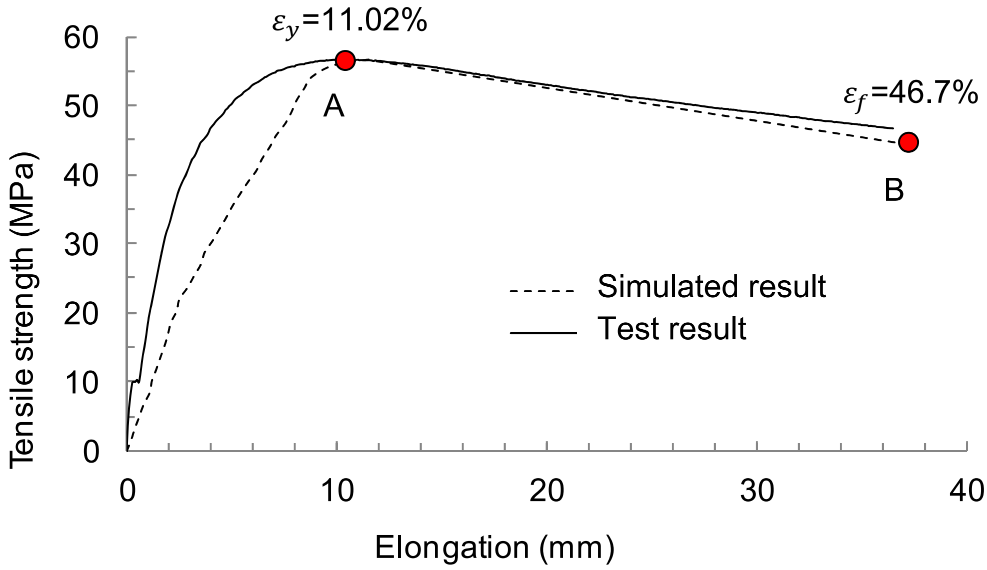

Fig. 3. Tensile strength of geocell specimen.

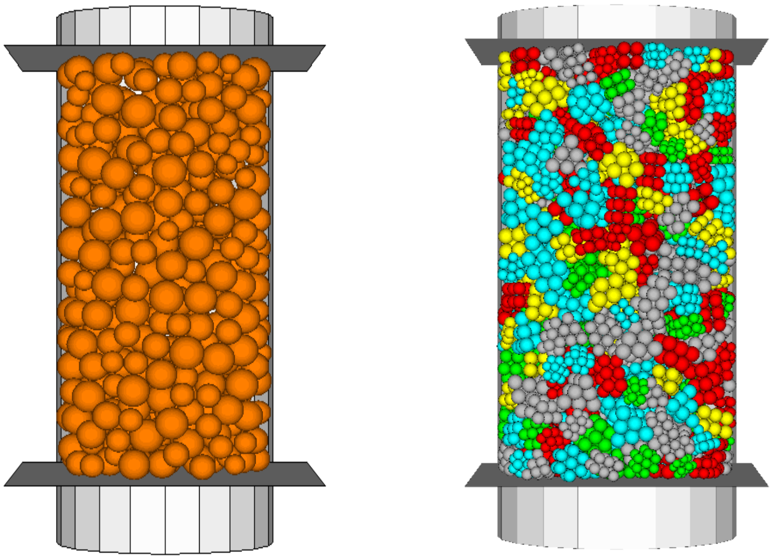

(a) (b)

Fig. 4. Triaxial test specimen simulated by: (a) spheres; (b) clumps.

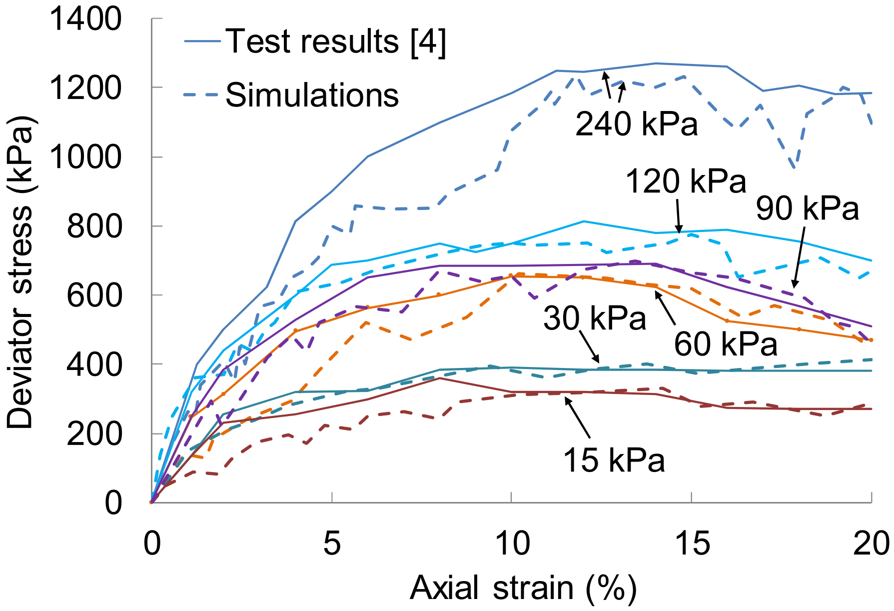

(a)

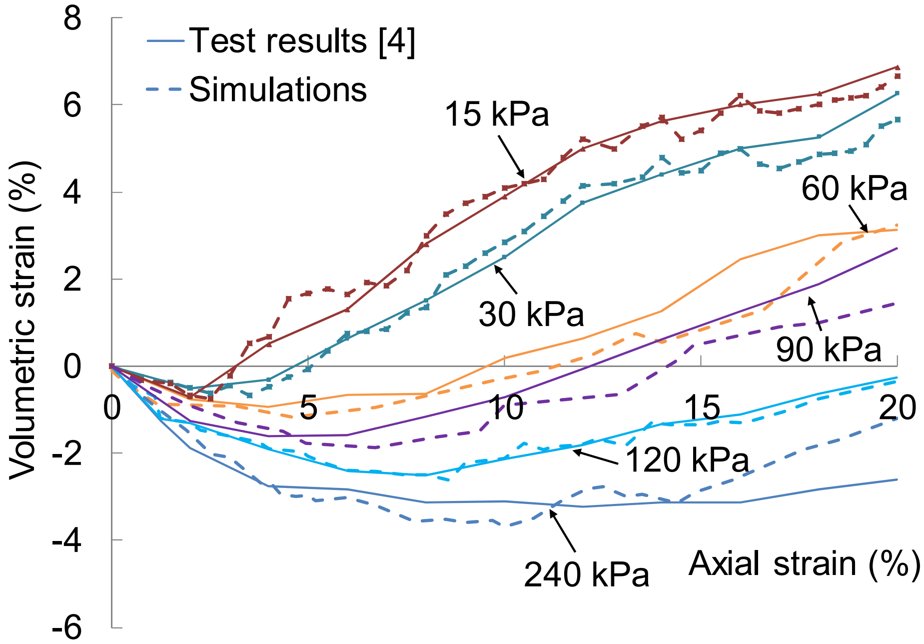

(b)

Fig. 5. Triaxial compression test results: (a) deviator stress vs. axial strain; (b) volumetric strain vs. axial strain.

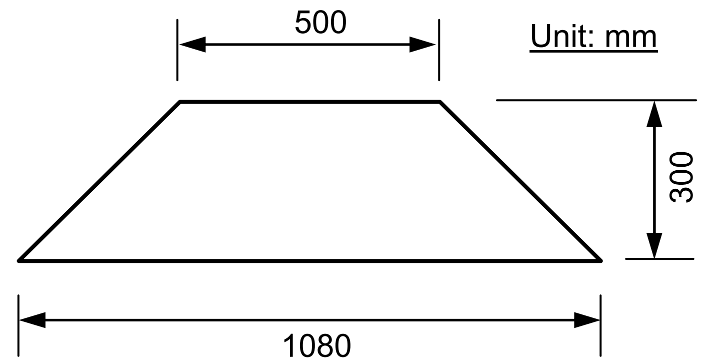

(a)

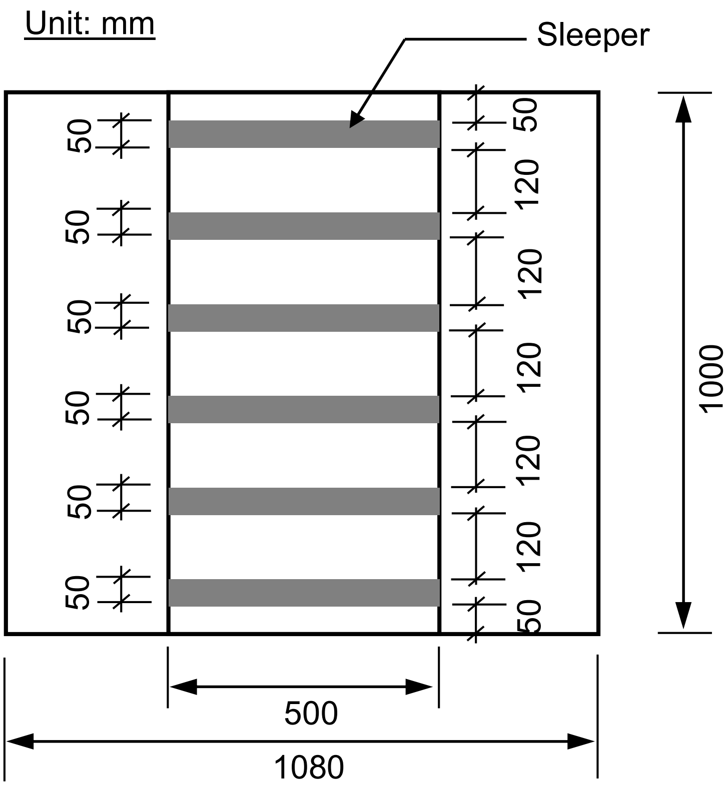

(b)

Fig. 6. Straight embankment: (a) cross section; (b) plan view.

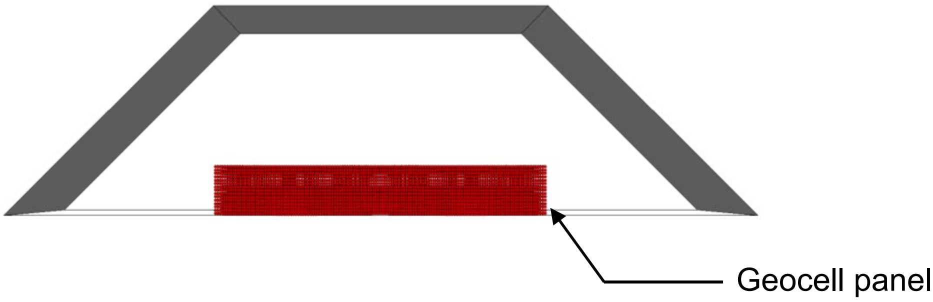
Geocell panel

(a)

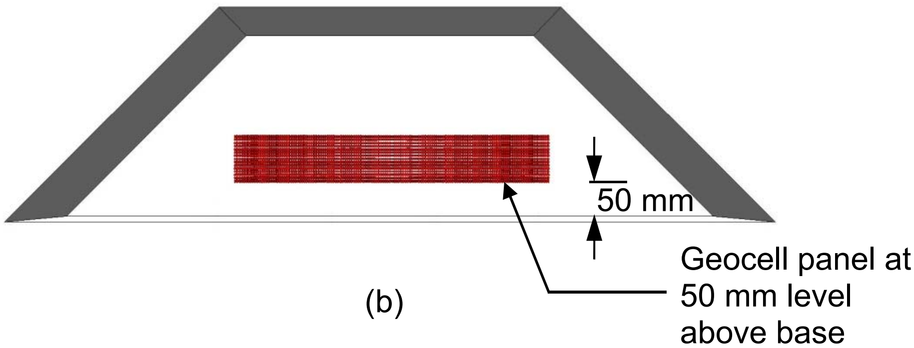
50 mm
Geocell panel at
50 mm level
above base

(b)

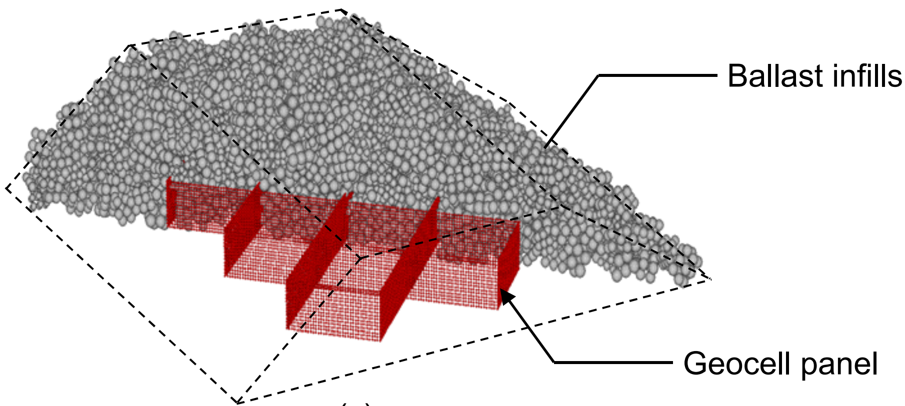
Ballast infills
Geocell panel

(c)

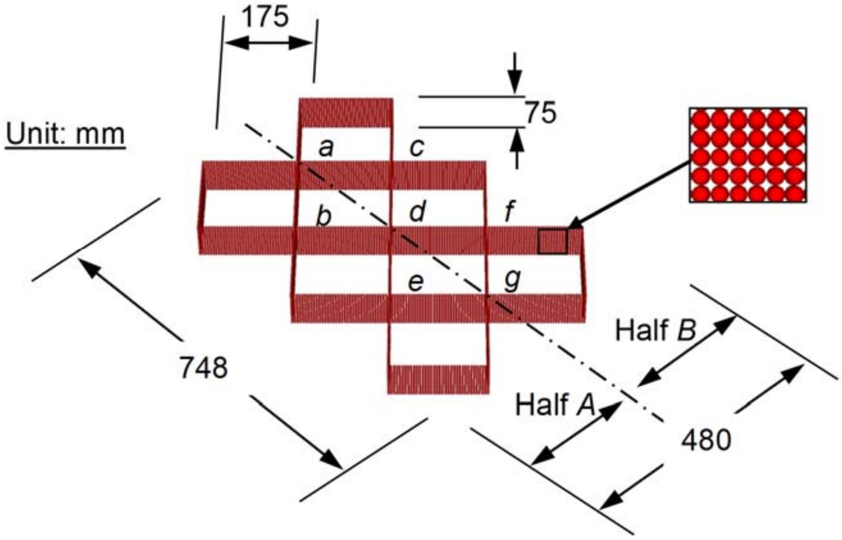

(d)

Fig. 7. Geocell panel: (a) at embankment base; (b) 50 mm above the base; (c) 3D perspective: infilled with ballast; and (d) 3D perspective: simulated using spheres.

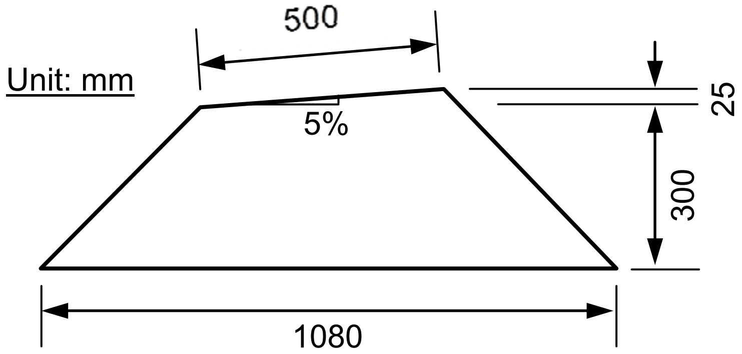

Fig. 8. Curved embankment cross section.

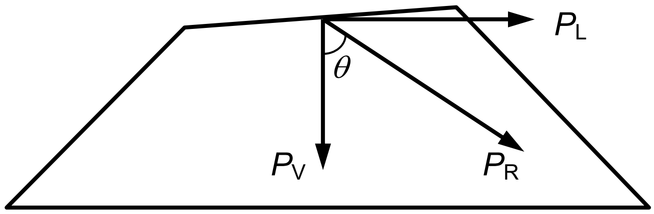

Fig. 9. Forces acted on curved embankment.

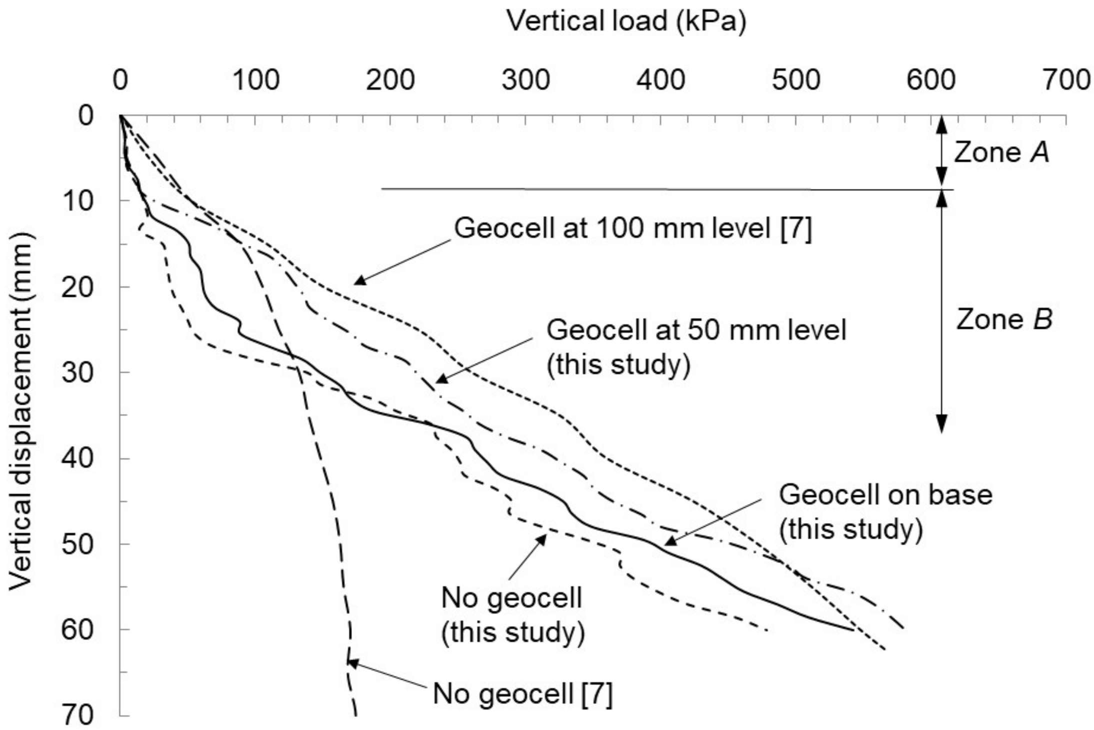

Fig. 10. Vertical displacement for straight embankment under monotonic loading.

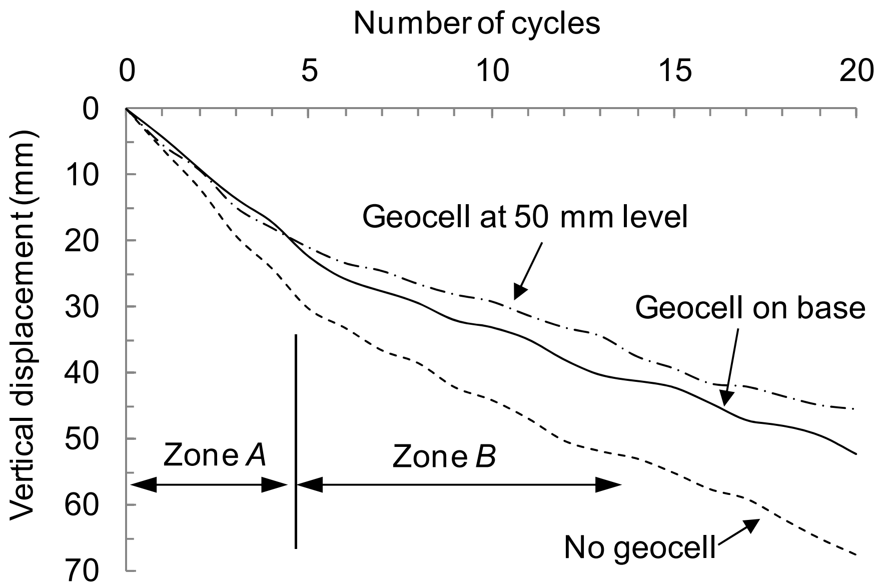

Fig. 11. Vertical displacement for straight embankment under cyclic loading.

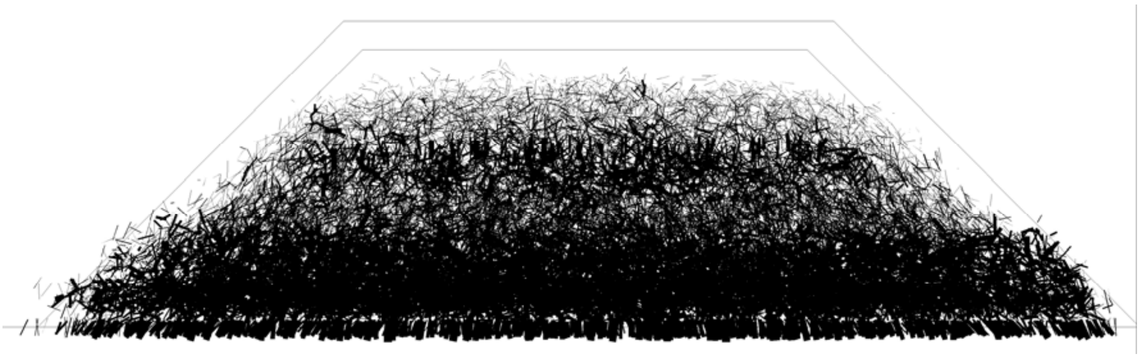

Max. Contact Force: 7.55 × 10^6 N Average Contact Force: 4.77 × 10^5 N

(a)

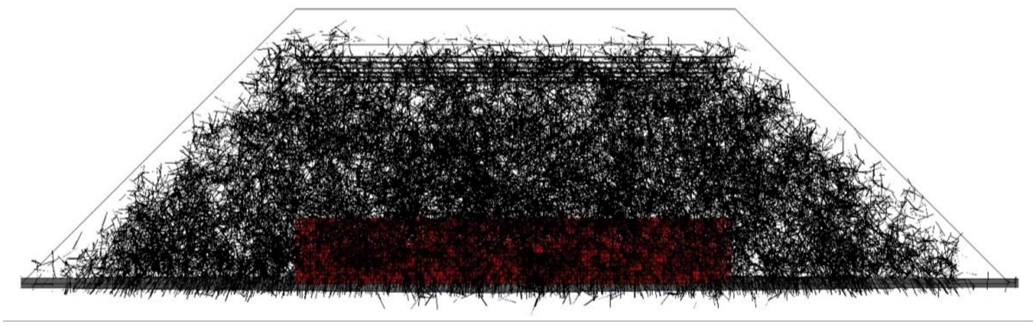

Max. Contact Force: 8.74 x 10^6 N Average Contact Force: 5.34 x 10^5 N

(b)

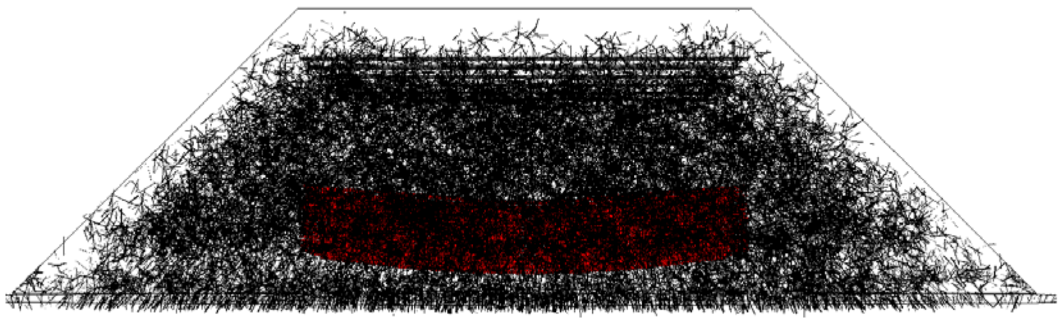

Max. Contact Force: 9.95 x 10^6 N Average Contact Force: 6.28 x 10^5 N

(c)

Fig. 12. Contact forces drawn at the same scale for straight embankment after the 20th cycle: (a) unreinforced; (b) geocell at base; and (c) geocell 50 mm above the base.

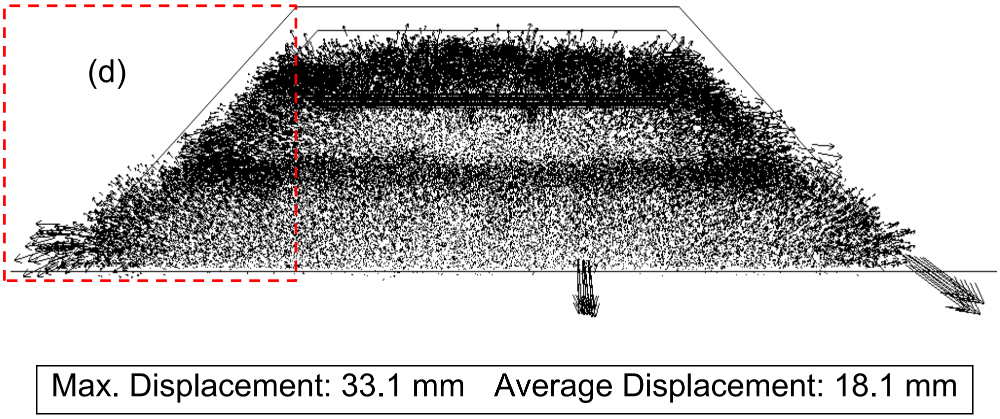
(d)
Max. Displacement: 33.1 mm Average Displacement: 18.1 mm
(a)

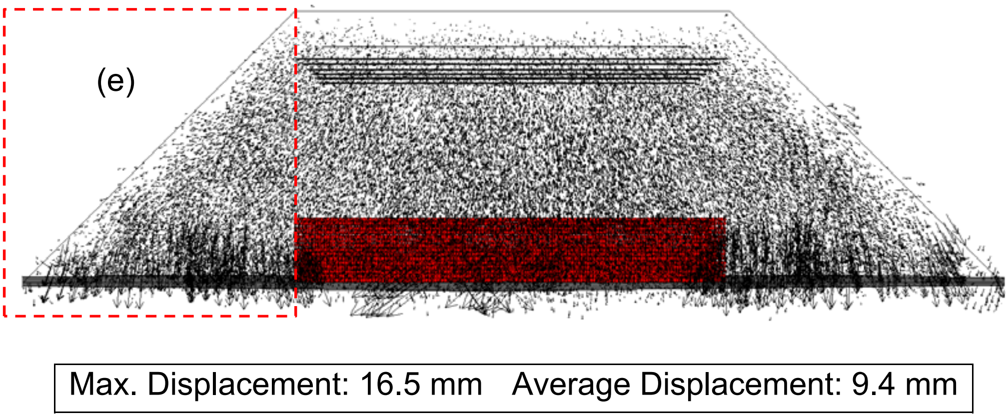
(e)
Max. Displacement: 16.5 mm Average Displacement: 9.4 mm
(b)

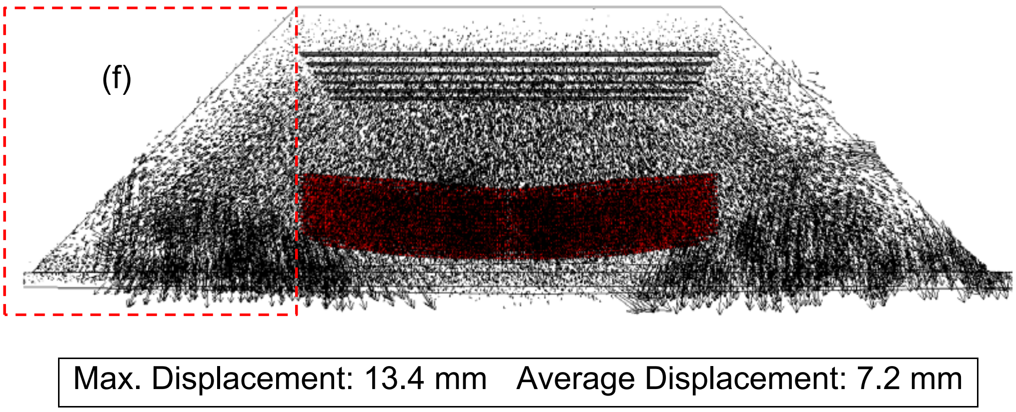
(f)
Max. Displacement: 13.4 mm Average Displacement: 7.2 mm
(c)

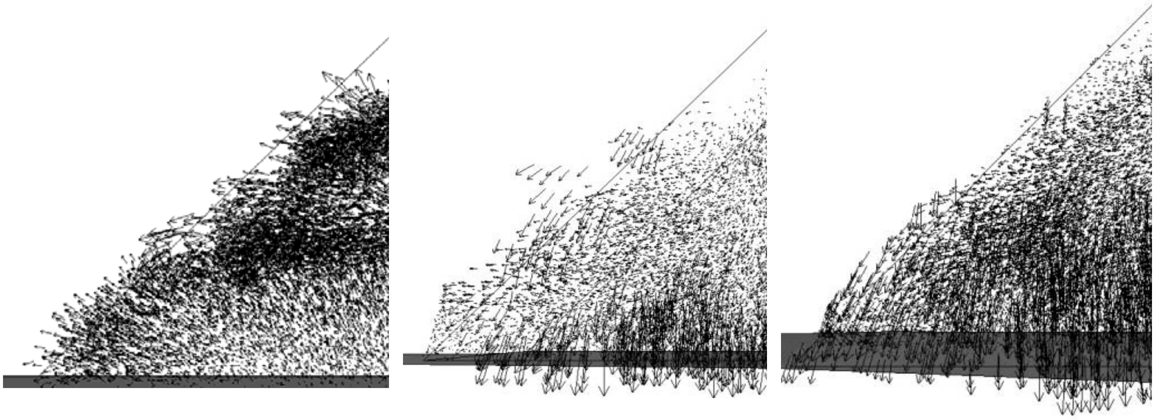

(d) (e) (f)

Fig. 13. Total displacment vectors drawn at the same scale for straight embankment after the 20th cycle: (a) unreinforced; (b) geocell at base; (c) geocell 50 mm above the base; (d–f) zoomed-in views of the left-hand-side unreinforced sections of three embankments.

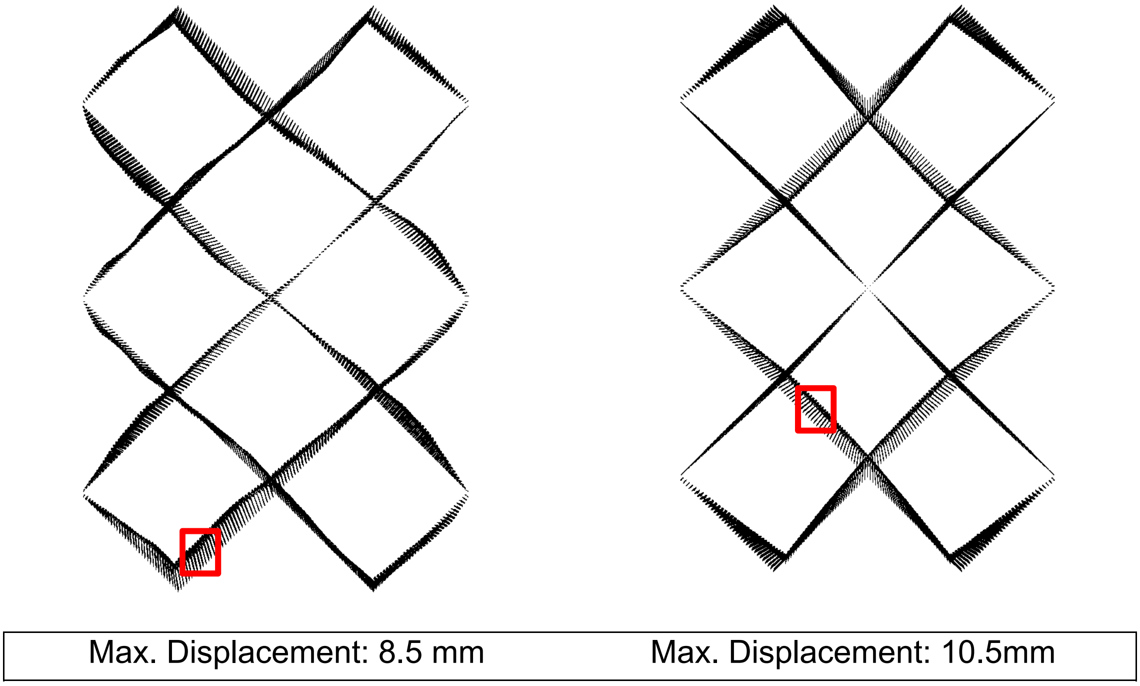

(a) (b)

Fig. 14. Total displacement vectors drawn at the same scale for geocell panel after the 20th cycle: (a) geocell on base; (b) geocell at 50 mm above the base.

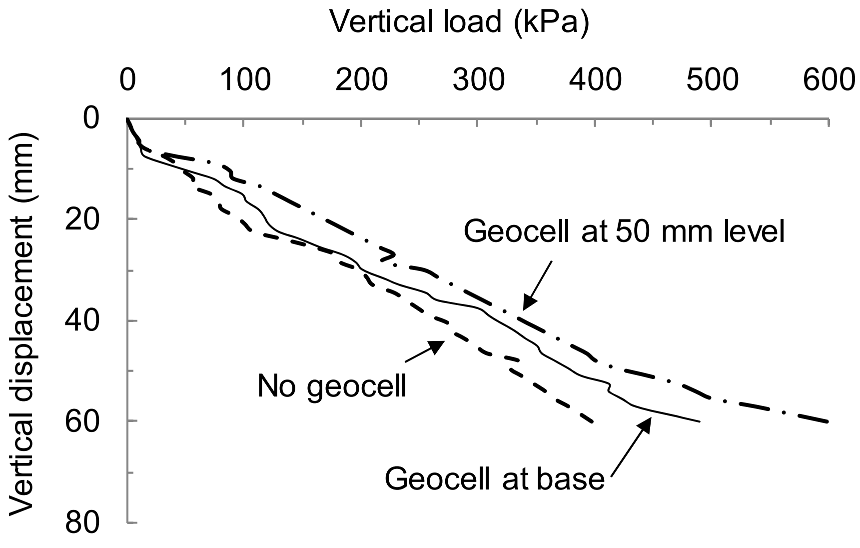

(a)

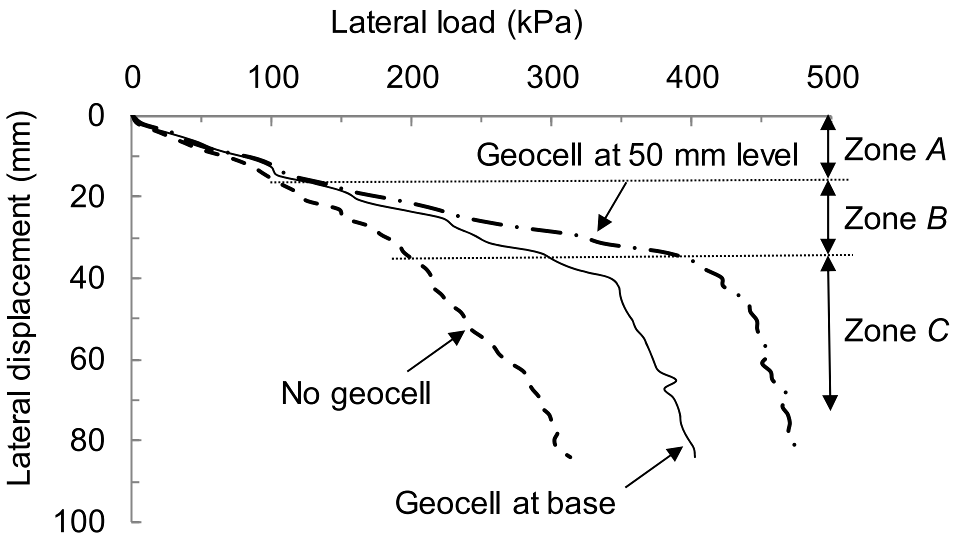

(b)

Fig. 15. Monotonic loading-induced sleepers movement in curved embankment: (a) Vertical displacement, (b) lateral displacement.

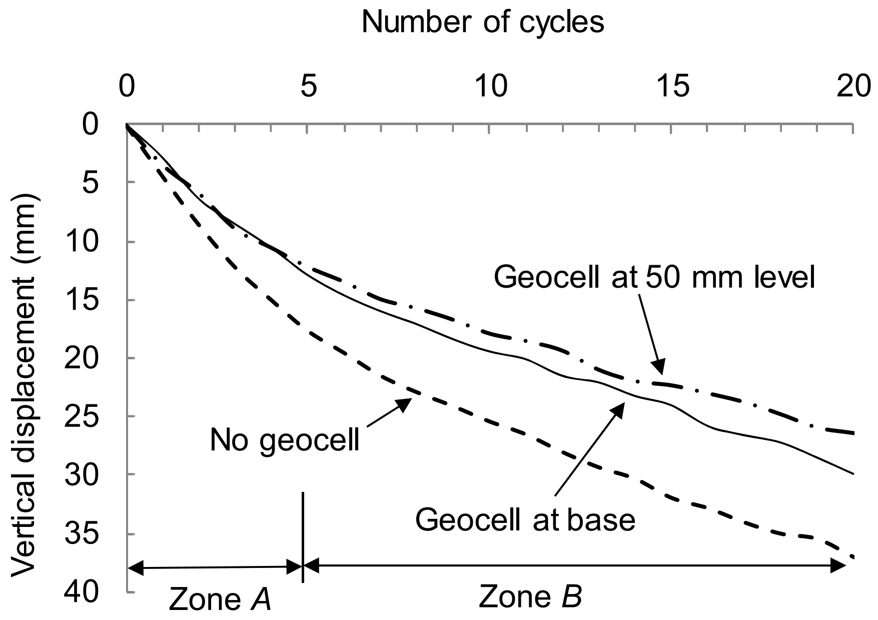

(a)

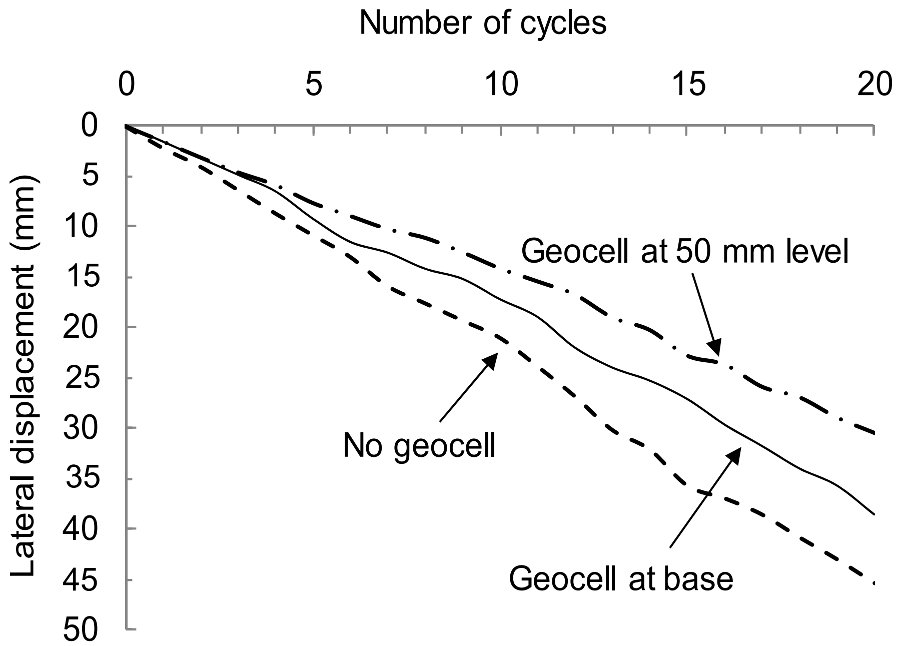

(b)

Fig. 16. Cyclic loading-induced sleepers movement in curved embankment: (a) vertical displacement; (b) lateral displacement.

Max. Contact Force: 8.73×10^6 N   Average Contact Force: 4.74×10^5 N

(a)

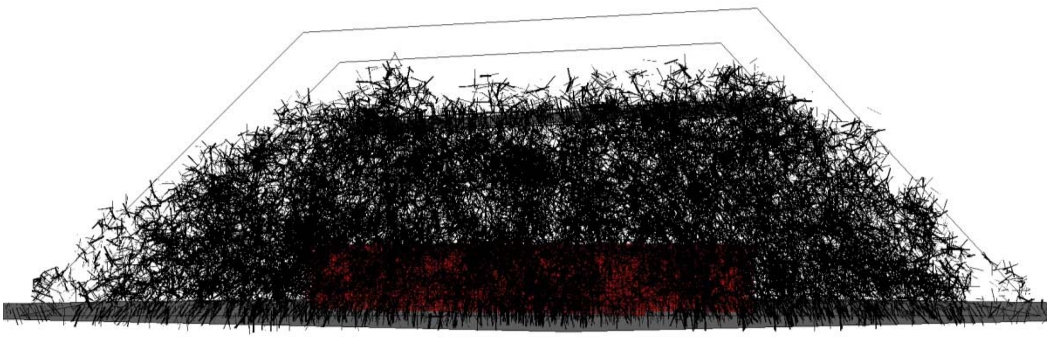

Max. Contact Force: 9.38×10^6 N   Average Contact Force: 6.28×10^5 N

(b)

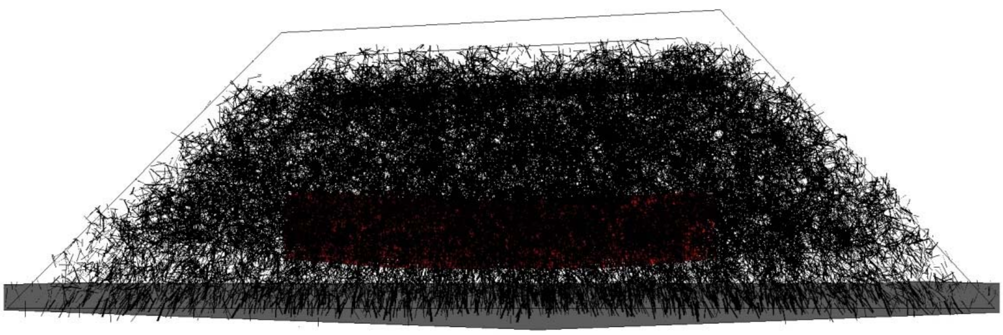

Max. Contact Force: 1.23×10^7 N   Average Contact Force: 8.51×10^6 N

(c)

Fig. 17. Contact forces drawn at the same scale for the curved embankment after the 20th cycle: (a) unreinforced; (b) geocell at base; and (c) geocell 50mm above the base.

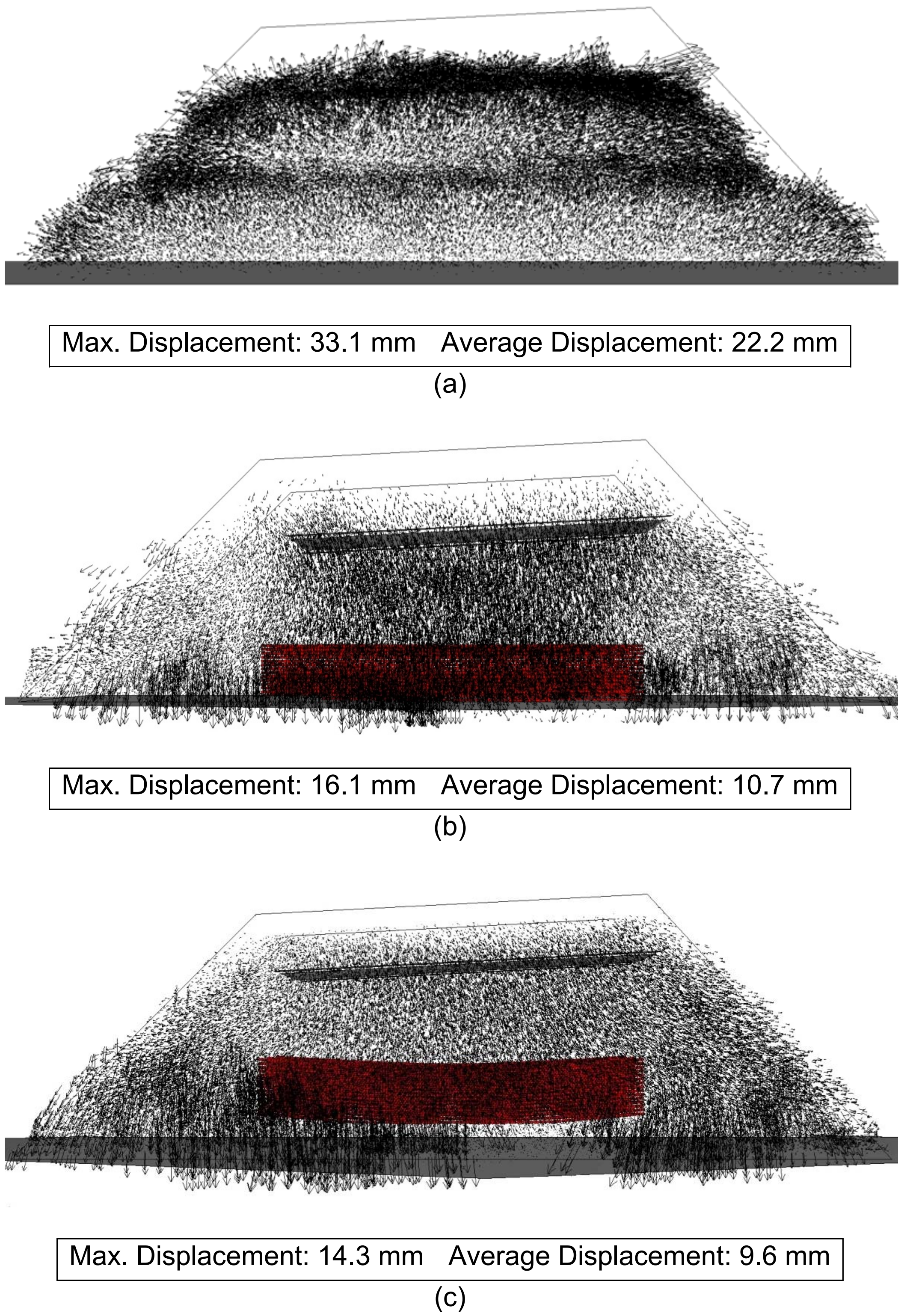

Fig. 18. Total displacment vectors drawn at the same scale for the curved embankment after the 20th cycle: (a) unreinforced; (b) geocell at base; and (c) geocell 50mm above the base.

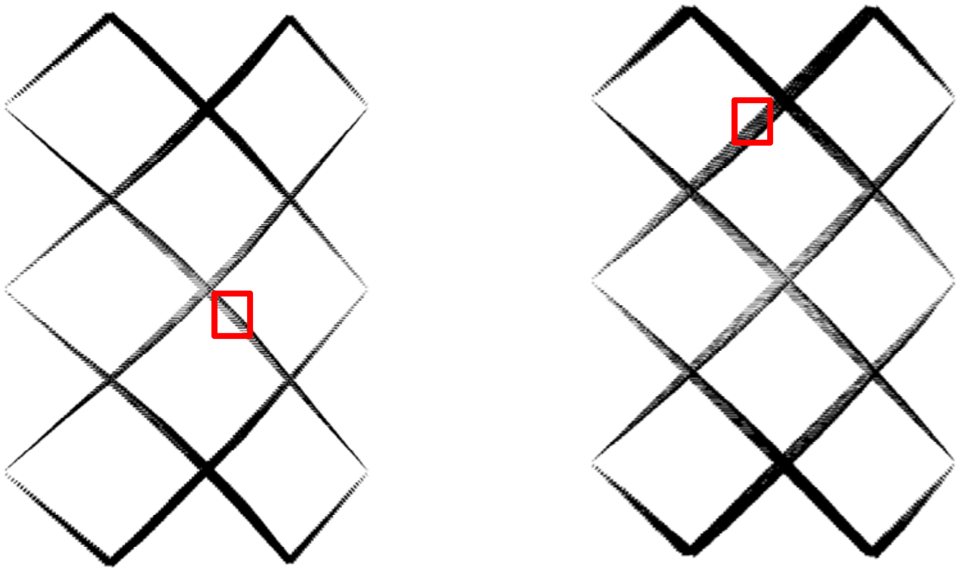

Max. Displacement: 7.7 mm	Max. Displacement: 11.4 mm
(a)	(b)

Fig. 19. Total displacment vectors drawn at the same scale for geocell panel after the 20^{th} cycle: (a) geocell on base; (b) geocell at 50 mm above the base.

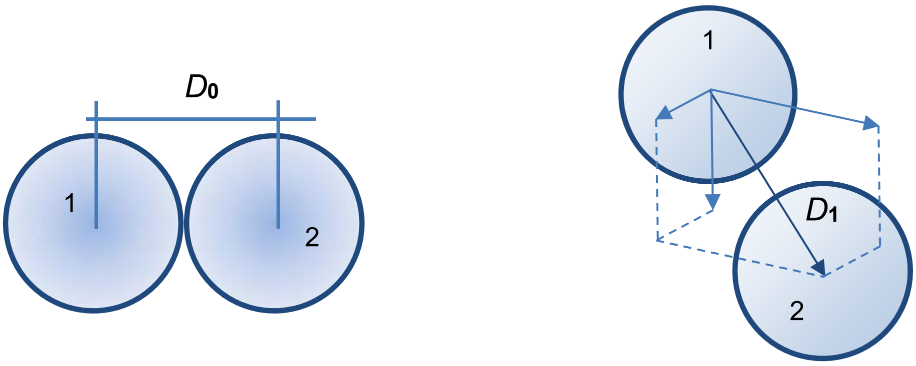

$$\varepsilon = \frac{(D_1 - D_0)}{D_0} \times 100\%$$

(a) (b)

Figure 20 Illustration on the calculation methodology of strain in geocell: (a) before displacement; (b) after displacement.

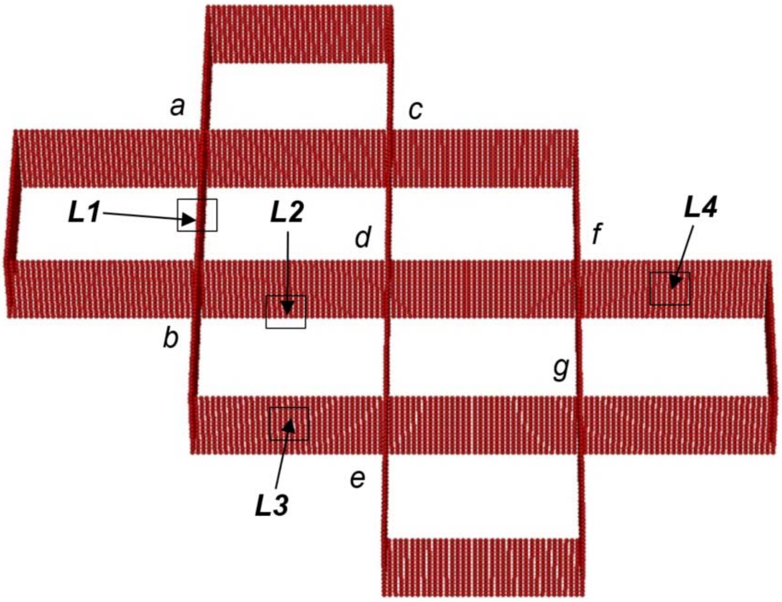

Figure 21 Locations of maximum strain.

Tables

Table 1. Micro-properties for geocell

Micro-property	Value
Density ρ (kg/m^3)	1.0×10^3
Normal stiffness k_n (N/m)	3.2×10^3
Shear stiffness k_s (N/m)	3.2×10^3
Parallel-bond normal stiffness $\overline{k}_n$ (N/m^3)	2.8×10^4
Parallel-bond shear stiffness $\overline{k}_s$ (N/m^3)	4.5×10^4
Parallel-bond normal strength $\overline{\sigma}_c$ (N/m^2)	6.8×10^4
Parallel-bond shear strength $\overline{\tau}_c$ (N/m^2)	6.5×10^4
Parallel-bond radius $\overline{R}$ (mm)	2.5
Tensile strength $\overline{\sigma}_t$ (N/m^2)	5.598×10^4
Softening stiffness $\hat{k}_s$ (N/m^3)	2.75×10^4
Normal stiffness in tension $\hat{k}_n$ (N/m)	3.2×10^4
Friction coefficient μ	0.3

Table 2. Clump templates developed for ballast

Clump template	Geometry	Number of spheres
Trapozoidal	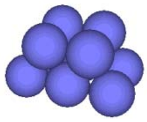	10
Triangular	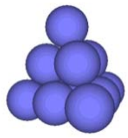	10
Rectangular	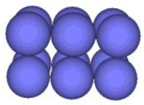	12
Hexagonal	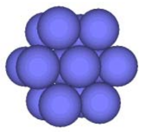	14

Table 3. Micro-properties for ballast clumps

Micro-property	Value
Density ρ (kg/m^3)	2.5×10^3
Normal stiffness k_n (N/m)	5×10^9
Shear stiffness k_s (N/m)	5×10^9
Parallel-bond normal stiffness $\overline{k}_n$ (N/m^3)	1.8×10^5
Parallel-bond shear stiffness $\overline{k}_s$ (N/m^3)	1.8×10^5
Parallel-bond normal strength $\overline{\sigma}_c$ (N/m^2)	6×10^{10}
Parallel-bond shear strength $\overline{\tau}_c$ (N/m^2)	6×10^{10}
Parallel-bond radius $\overline{R}$ (mm)	1.0
Frictional coefficient μ	1.0

Table 4. Geocell panel strains

	Strain (%)			
	Monotonic loading		Cyclic loading	
Position	Geocell at base	Geocell 50 mm above base	Geocell at base	Geocell 50 mm above base
Junction *a*	29.1	34.1	10.9	11.3
Junction *b*	39.2	39.8	15.6	14.8
Junction *c*	39.2	21.1	18.7	18.3
Junction *d*	24.1	29.7	13.3	13.4
Junction *e*	30.2	38.9	12.0	10.2
Junction *f*	41.6	41.2	18.0	15.3
Junction *g*	26.9	33.0	16.2	10.0
Panel half *A*	18.9	35.3	19.8	16.1
Panel half *B*	24.4	39.1	27.0	22.7
Maximum strain	39.7	45.5	28.4	23.4